Phenomenological three-parameter nucleon-nucleon potential for symmetric nuclei ($N=Z$) from $Z=2$ to infinity

A. E. Pozamantir and A. W. Overhauser
Department of Physics, Purdue University, West Lafayette, Indiana 47907-1396
(Received 29 July 1999; published 4 June 2001)

In order to study collective instabilities in symmetric nuclear matter, a simple phenomenological nucleon-nucleon finite-range potential with three adjustable parameters is proposed. The three parameters are the attractive strength, the attractive range, and the (zero range) repulsive strength. The potential reproduces the binding energy, equilibrium density, compressibility modulus, and the effective mass of nuclear matter, as well as the binding energies of ^{4}He, ^{16}O, and ^{40}Ca. The latter conditions are crucial for preventing spurious ''quasicrystallization'' effects in nuclear matter. With this potential and a $(2+1)$-D deformed oscillator basis, variational Hartree-Fock calculations extending over the configuration space of the lowest 55 orbitals were performed for spin-zero, isospin-zero light nuclei up to $A=80$. Large ground-state deformations and exotic nuclear shapes were found for many nuclei. Implications for their rotational spectra are discussed.

DOI: 10.1103/PhysRevC.64.014302 PACS number(s): 21.60.Jz, 21.10.Re, 21.10.Dr, 21.10.Gv

I. INTRODUCTION

The Hartree-Fock (HF) approximation has proved to be a reasonably good way of describing the ground state and collective properties of nuclei, especially the heavy ones. Often, this approximation is expressed as a variational principle for the ground-state energy and the one-particle excited states of a system of fermions. Systematic HF calculations require an effective two-body nuclear potential. Because of the inherent complexity of these calculations, it is desirable for the potential to have as simple a structure as possible. The calculations described below included evaluation of the energies for more than 3×10^6 Slater determinants (having dimensions up to 80×80). Rather than being derived from a realistic two-body force (with some additional higher-order phenomenological corrections), such a potential involves direct parametrization of the effective nuclear force. Its validity relies on its ability to reproduce the accepted values of the parameters of infinite nuclear matter (binding energy, compressibility modulus, mean density, etc.) along with the rms radii and binding energies of light nuclei, for which the surface energy is the dominant correction.

A popular choice of an effective nuclear interaction is the Skyrme potential [1] and its many modifications [2–5]. Its main attractiveness lies in the zero-range radial dependence given by the δ functions, which considerably simplifies the calculation of matrix elements. The three-body force correction also has zero-range and is expressed through a density-dependent term. The physical content of the Skyrme interaction, however, suffers from this simplification as there is no natural way to include the surface energy in a finite nuclear system. [Instead the surface energy is modeled by an *ad hoc* $(\nabla\rho)^2$ term.] Many-body effects are expressed by a density-dependent (repulsive) term that, for properly chosen parameters, has an unexpectedly high value for nuclear matter ($\sim$22 MeV/nucleon [3] or $\sim$18 MeV/nucleon [5]), values that are comparable with the average kinetic energy per nucleon. In contrast, studies by Kasahara, Akaichi, and Tanaka [6] show that the three-body-force contribution to the binding energy of nuclear matter is only 3 or 4 MeV/nucleon.

A more satisfying approach consists in using a finite-range attractive potential [7–14]. The finite range of such an interaction is a phenomenological substitute for one-pion (long-range) and two-pion (intermediate-range) exchange processes. Sometimes [9], a short-range cutoff parameter is introduced to model the repulsive core of the interaction, instead of an explicit velocity-dependent repulsion. These semirealistic potentials go one step further than Skyrme potentials as they are able to reproduce reasonably well not only the ground-state properties of nuclei and nuclear matter, but also the experimental data on nucleon-nucleon low-energy ($\leqslant$300 MeV) scattering. The finite range gives rise in a natural way to the surface energy of finite nuclei. [*Ad hoc* $(\nabla\rho)^2$ terms are unnecessary.] Any improvement over the Skyrme interaction comes at a price. In these potentials, the radial dependence is cast in the Yukawa form [$\sim\exp(-r/a)/(r/a)$], as in the Seyler-Blanchard and the Reid potentials [7,8], in the Gaussian form [$\sim\exp(-r^2/a^2)$], as in the Gogny potential [10], or as a combination of the two [9,12]. Matrix element calculations become a daunting task, in some cases prohibitively so [15]. An attempt to fit both scattering data and nuclear ground-state properties necessitates seven or more adjustable parameters.

In this paper, we propose a simple, finite-range effective nucleon-nucleon potential having only three adjustable parameters. Applied to even-even, $N=Z$ nuclei, the potential retains only a central (radial) part and consists of two terms: an attractive and a repulsive one. The attractive term has a modified Gaussian form with a single range parameter s; and the repulsive term has a zero-range (δ-function) radial dependence. Nuclear saturation is achieved by letting the strength of the repulsive term be proportional to the square root of the ''average kinetic energy.'' The three parameters, the attractive strength, the repulsive strength, and the range, are determined by fitting simultaneously the binding energy and mean density of nuclear matter as well as the binding energy of the alpha particle. The three parameters are intended only as

many-body phenomenological parameters, and no attempt is made to fit two-body scattering data. The potential has a simple mathematical structure that allows for extended HF variational calculations. [In our case we were able to use the entire configuration space of the $(2+1)$-dimensional quantum oscillator with the 2-D main quantum number n ranging from 0 to 5, and the 1-D main quantum number m ranging from 0 to 7, m and n outside these ranges generate only highly excited configurations.]

Our primary interest in the potential lies in its subsequent application to studying collective instabilities in symmetric nuclear matter. To this end, we completely neglect Coulomb, spin-orbit, tensor, and pairing interactions, which play no role in symmetric nuclear matter. At the same time, it is essential that the proposed potential reproduce correctly the nuclear part of the binding energies of finite symmetric nuclei (^{4}He, ^{16}O, ^{40}Ca, etc.). Satisfying this requirement means that the surface energy—the dominant correction to B_∞ (the binding energy of nuclear matter)—is automatically reproduced for light nuclei, where it is relatively most important. For example, too large a value for the binding energy of ^{4}He would lead to a spurious ''quasicrystallization.'' of symmetric nuclear matter, which would then break up into a collection of alpha-particle-like clusters.

Within the restricted basis set of a deformed $(2+1)$-dimensional linear quantum oscillator model, binding energies were computed and compared with experimental values for even-even, $N=Z$ nuclei for A between 4 and 80. The effects of closed oscillator shells on binding energy is clearly seen for ^{4}He, ^{16}O, ^{40}Ca, and ^{80}Zr. This qualitative agreement is gratifying given the oversimplified nature of the model potential. Nevertheless, the potential reproduces all nuclear matter properties as well as the binding energies of ^{4}He, ^{16}O, and ^{40}Ca, which lends credibility to our subsequent studies of collective instabilities in nuclear matter [16], since the surface energy is then accounted for *ab initio*.

The $(2+1)$-D oscillator model allows us to study shape excitations of light nuclei in which rearrangement of several nucleons occurs simultaneously. Such an excitation would be expected to have a longer half-life than a one-particle excitation; and it is often accompanied by a significant change in shape. ''Dot diagrams'' for the $(2+1)$-D oscillator model are introduced and used in the search for the ground state and shape excitations of $N=Z$, even-even nuclei. Collective nuclear deformations, isomeric (long-lived) states of light nuclei, and low-lying transitions are discussed. Although in what follows more than 4000 Slater determinants are optimized, this number is but a small fraction of the numerable energy levels.

II. THE POTENTIAL AND THE STATISTICAL APPROXIMATION

The proposed nucleon-nucleon potential has the form

$$V(\mathbf{r}_1,\mathbf{r}_2)=-\alpha C(\mathbf{r}_1-\mathbf{r}_2)^2 e^{-(\mathbf{r}_1-\mathbf{r}_2)^2/s^2}+\beta\sqrt{\langle T\rangle}\,\delta(\mathbf{r}_1-\mathbf{r}_2), \tag{1}$$

where $\langle T\rangle$ is the [center-of-mass (c.m.) motion corrected] average kinetic energy given by

$$\langle T\rangle=\frac{1-1/A}{A}\sum_{i=1}^{A} t_i, \tag{2}$$

with t_i being the kinetic energy of the ith nucleon, and $A=2N=2Z$, the total number of nucleons. Equation (2) is exact for a Slater determinant of localized orbitals, i.e., in the HF approximation. C is the normalization coefficient of the modified Gaussian

$$C=(\tfrac{3}{2}\pi^{3/2}s^5)^{-1}. \tag{3}$$

Saturation of the nuclear density is achieved by letting the n-n repulsion increase with increasing $\langle T\rangle$. Compared with a two-nucleon velocity-dependent Skyrme repulsion together with a density-dependent Skyrme repulsion, the repulsive term of Eq. (1) provides a simpler way to represent core penetration of nucleon pairs. It would not be appropriate to calculate $\langle T\rangle$ by means of a Thomas-Fermi approximation involving the density ρ. Such an approach leads to a nucleon-effective mass (in nuclear matter) given by $\mu^*/\mu=1$. We find instead that, by calculating $\langle T\rangle$ accurately, $\mu^*/\mu=0.41$, similar to values obtained by other workers.

A simpler form of the potential would have been,

$$V(\mathbf{r}_1,\mathbf{r}_2)=-\alpha' C' \exp[-(\mathbf{r}_1-\mathbf{r}_2)^2/s^2]+\beta'\langle T\rangle\delta(\mathbf{r}_1-\mathbf{r}_2), \tag{4}$$

and it was also studied. This potential can fit the binding energy and density of nuclear matter as well as the binding energy of ^{4}He. However, the binding energy of ^{16}O is then found to be too large by about 2 MeV/nucleon, which means its surface energy is too small. Inclusion of the $(\mathbf{r}_1-\mathbf{r}_2)^2$ factor in the attractive part of Eq. (1) solves this problem. Multiplying the repulsive term by $\langle T\rangle$ instead of $\sqrt{\langle T\rangle}$ leads to a compressibility modulus for nuclear matter substantially higher than 300 MeV. Recent experimental studies indicate a modulus nearer to 200 MeV, and we obtain below a value of 225 MeV.

By confining our attention to even-even, $N=Z$ nuclei we avoid the necessity of having a tensor force. Each spatial orbital is filled with four nucleons, so the average of the tensor operator

$$\mathbf{S}_{12}=3(\boldsymbol{\sigma}_1\cdot\hat{\mathbf{r}})(\boldsymbol{\sigma}_2\cdot\hat{\mathbf{r}})-(\boldsymbol{\sigma}_1\cdot\boldsymbol{\sigma}_2) \tag{5}$$

is zero regardless of the nuclear shape.

The three adjustable parameters, α, β, and s, are fixed by the three following conditions:

$$B(^4\mathrm{He})=7.3\,\mathrm{MeV};\quad B_\infty=15\,\mathrm{MeV};\quad \left.\frac{\partial B_\infty}{\partial\rho}\right|_{R_0=1.1\ \mathrm{fm}}=0. \tag{6}$$

Here $B(^4\mathrm{He})$ is the Coulomb-corrected binding energy per nucleon of the alpha particle, B_∞ is the binding energy per nucleon in nuclear matter, and R_0 is the radius of a sphere that contains one nucleon at the equilibrium density of

nuclear matter. The reason why B_∞ has been taken to be 15 MeV is explained in Ref. [16]. An additional ~1 MeV of binding arises from a density instability in nuclear matter. On account of the normalizing factor C in Eq. (1), the range parameter s does not enter the calculation of B_∞ (for uniform nuclear matter). The last two equations of Eq. (6) are therefore decoupled from the first one. α and β can then be determined as follows. We may write

$$B_\infty = |\langle T\rangle + \langle V_\alpha\rangle + \langle V_\beta\rangle|. \tag{7}$$

$\langle V_\alpha\rangle$ is the average expectation value of the α-term in the potential. It includes both direct and exchange terms. On account of complications that arise when calculating exchange integrals of a finite-range potential, we evaluate them here in a statistical approximation, which is the exact result for uniform matter. We first calculate the exchange energy between two nucleons described by plane waves (normalized in the volume, V) with wave vectors $\mathbf{k}$ and $\mathbf{k}'$:

$$g_\alpha(\mathbf{k},\mathbf{k}') = \alpha C \frac{1}{V^2}\int d^3r\, d^3r'\, e^{i(\mathbf{r}-\mathbf{r}')(\mathbf{k}'-\mathbf{k})}(\mathbf{r}-\mathbf{r}')^2 \times \exp[-(\mathbf{r}-\mathbf{r}')^2/s^2]. \tag{8}$$

Upon substituting $\boldsymbol{\rho}=\mathbf{r}-\mathbf{r}'$ and $\mathbf{q}=\mathbf{k}-\mathbf{k}'$, we find,

$$g_\alpha(\mathbf{q}) = \alpha C \frac{1}{V}\int d^3\rho\, e^{i(\boldsymbol{\rho}\cdot\mathbf{q})}\rho^2 e^{-\rho^2/s^2} = \alpha \frac{1}{V} e^{-(1/4)q^2s^2}(1-\tfrac{1}{6}q^2s^2). \tag{9}$$

Following Overhauser and co-workers [17,18], we average $g_\alpha(q)$ over the Fermi sphere of occupied states using geometric probability techniques. With four different species of particles ($p\uparrow, p\downarrow, n\uparrow, n\downarrow$), we obtain

$$\langle g_\alpha(q)\rangle = \frac{1}{4}\int_0^{2k_F} dq\, P(q) g_\alpha(q), \tag{10}$$

where

$$P(q) = 3\frac{q^2}{k_F^3} - \frac{9}{4}\frac{q^3}{k_F^4} + \frac{3}{16}\frac{q^5}{k_F^6} \tag{11}$$

is the geometric probability of two randomly chosen points in a sphere of radius k_F having a separation q. Obviously, $q \leqslant 2k_F$. Combining Eqs. (9), (10) and (11), one finds

$$\langle g_\alpha(q)\rangle = \alpha \frac{1}{V} g_s(k_F), \tag{12}$$

with

$$g_s(k_F) \equiv \frac{1}{2s^6k_F^6}[-6+3s^2k_F^2+3(2+s^2k_F^2)e^{-s^2k_F^2}]. \tag{13}$$

This dimensionless exchange function can be rewritten using

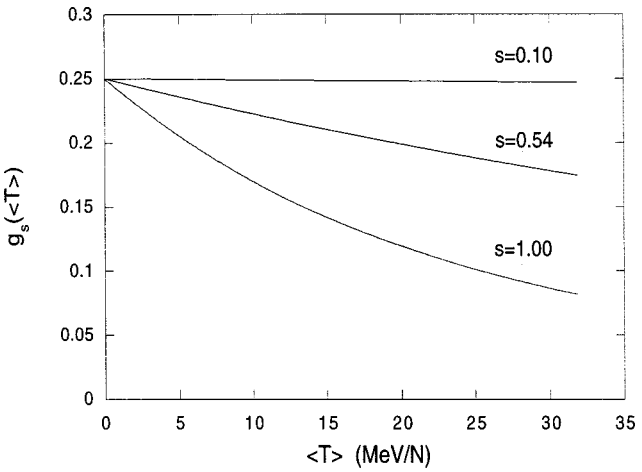

FIG. 1. The exchange function $g_s(\langle T\rangle)$ for different values of the range parameter s.

$$\langle T\rangle = \frac{3}{5}\frac{\hbar^2k_F^2}{2\mu}, \quad \mu \equiv \tfrac{1}{2}(m_p+m_n), \quad a \equiv \frac{10\mu}{3\hbar^2}, \quad b \equiv as^2, \tag{14}$$

as

$$g_s(\langle T\rangle) = \frac{1}{2b^3\langle T\rangle^3}[-6+3b\langle T\rangle+3e^{-b\langle T\rangle}(2+b\langle T\rangle)]. \tag{15}$$

The exchange function g_s is shown in Fig. 1 for different values of the range parameter s. As expected, in the limit $s \to 0$, the exchange function becomes 1/4, the exact result, independent of $\langle T\rangle$. For practical applications, it is convenient to approximate the exchange function (15) with a parabolic fit having the form

$$g_s^{\text{appr}}(\langle T\rangle) = \tfrac{1}{4} + c_1\langle T\rangle + c_2\langle T\rangle^2. \tag{16}$$

If one plots this approximate function g_s^{appr} with c_1 and c_2 obtained from the exact values of $g_s(\langle T\rangle)$ at two points, $\langle T\rangle = 10$ and 20 MeV, for $s = 0.54$ (our actual interaction range), Eq. (16) is indistinguishable from the exact curve $g_{0.54}(\langle T\rangle)$ of Fig. 1.

Consider now the first term of Eq. (1) and the pure plane-wave states, $\varphi_{\mathbf{k}}(\mathbf{r}) = e^{i\mathbf{kr}}/\sqrt{V}$, of nuclear matter. The direct term of Eq. (7) is

$$\langle V_\alpha\rangle^{\text{direct}} = \frac{1}{A}\left(-\frac{1}{2}\alpha\frac{A^2}{V}\right) = -\frac{1}{2}\alpha\rho, \quad \rho \equiv \frac{A}{V}. \tag{17}$$

Accordingly, the sum of the direct and exchange contributions is

$$\langle V_\alpha\rangle = -\tfrac{1}{2}\alpha\rho[1-g_s(\langle T\rangle)]. \tag{18}$$

In evaluating the expectation value of the repulsive term $\langle V_\beta\rangle$, the exchange term for parallel spin and parallel isospin will cancel exactly its corresponding direct term, owing to

the zero range of the repulsive δ function. The average repulsive energy is therefore the direct term multiplied by the factor 3/4,

$$\langle V_\beta \rangle = \tfrac{3}{4}(\tfrac{1}{2}\beta\rho\sqrt{\langle T\rangle}) = \tfrac{3}{8}\beta\rho\sqrt{\langle T\rangle}. \tag{19}$$

The average binding energy in nuclear matter is therefore

$$B_\infty = \left|\langle T\rangle - \tfrac{1}{2}\alpha\rho[1-g_s(\langle T\rangle)] + \tfrac{3}{8}\beta\rho\sqrt{\langle T\rangle}\right|, \tag{20}$$

where

$$\rho = (\tfrac{4}{3}\pi R_0^3)^{-1}, \quad \langle T\rangle = (\tfrac{9}{8}\pi)^{2/3}\frac{1}{aR_0^2}, \tag{21}$$

so the last two relations of Eq. (6) determine the strength of the attractive and repulsive terms of Eq. (1):

$$\alpha = 1690 \ \text{MeV fm}^3, \quad \beta = 255 \ \text{MeV}^{1/2}\,\text{fm}^3. \tag{22}$$

Now we can verify that other characteristics of nuclear matter are reproduced correctly. The compressibility modulus K, defined in terms of the mean nuclear radius is

$$K \equiv \left| R_0^2 \frac{\partial^2 B_\infty}{\partial R_0^2}\right|_{R_0 = 1.1 \ \text{fm}} = 225 \ \text{MeV}, \tag{23}$$

very close to values 210–220 MeV determined by Blaizot *et al.* [19] or 231 ± 5 MeV reported recently by Youngblood, Clark, and Lui [20]. The ratio of the effective nucleon mass to the free-nucleon mass, μ^*/μ, applicable to single-particle excitations near the Fermi surface, is readily obtained:

$$\frac{\mu^*}{\mu} = \left(1 + \tfrac{1}{2}\alpha\rho\frac{\partial g_s(\langle T\rangle)}{\partial\langle T\rangle} + \tfrac{3}{16}\beta\rho\langle T\rangle^{-1/2}\right)^{-1} \approx 0.41. \tag{24}$$

This effective mass is similar to values found in Refs. [7,10].

Finally, the range parameter s is determined by fitting the binding energy of the α-particle. We take the one-particle orbitals to be the wave function for the ground state of a 3-D oscillator of frequency ω:

$$\varphi(\mathbf{r}) = \left(\frac{\gamma}{\pi}\right)^{3/2} e^{-(1/2)\gamma r^2}, \quad \gamma \equiv \frac{\mu\omega}{\hbar}. \tag{25}$$

The center-of-mass-corrected average kinetic energy is $(9/16)\hbar\omega$. The four orbitals are identical, therefore the exchange energy is canceled exactly by the corresponding direct terms. The average interaction energy then becomes [see the Appendix, Eqs. (A38) and (A39)]

$$\langle V\rangle = \frac{1}{4}\sum_{i>j}\langle ij|V_{ij}|ij\rangle = \tfrac{3}{2}(W_\alpha + W_\beta), \tag{26}$$

with

$$W_\alpha = -\alpha\left(\frac{\gamma}{2\pi}\right)^{3/2}(1+\tfrac{1}{2}\gamma s^2)^{-5/2} \tag{27}$$

and

$$W_\beta = \tfrac{3}{4}\beta\left(\frac{\gamma}{2\pi}\right)^{3/2}(\hbar\omega)^{1/2}. \tag{28}$$

Using the notation of Eqs. (14) and (25), we put $\hbar\omega = \frac{10}{3}\gamma/a$. The binding energy per nucleon of the α-particle, with the parameters α and β given by Eq. (22), now depends on only two unknown parameters, γ and s:

$$B(^4\text{He}) = \left|\frac{15}{8}\frac{\gamma}{a} - \frac{3}{2}\alpha\left(\frac{\gamma}{2\pi}\right)^{3/2}(1+\tfrac{1}{2}\gamma s^2)^{-5/2} + \frac{9}{8}\beta\left(\frac{\gamma}{2\pi}\right)^{3/2}\left(\frac{10}{3}\frac{\gamma}{a}\right)^{1/2}\right|. \tag{29}$$

For a given s, $B(^4\text{He})_{\min}$ is obtained by maximizing Eq. (29) with respect to γ. After straight-forward numerical calculations, the two conditions

$$\frac{\partial B(^4\text{He})}{\partial\gamma} = 0 \ \text{ and } \ B(^4\text{He}) = 7.3 \ \text{MeV} \tag{30}$$

are satisfied with $\hbar\omega(=\hbar^2\gamma/\mu) = 17.4\,\text{MeV}$ and

$$s = 0.54 \ \text{fm}. \tag{31}$$

Equations (1), (22), and (31) completely specify the interaction potential.

III. VARIATIONAL PROCEDURE AND ''DOT DIAGRAMS''

All calculations below are made using a restricted HF variational procedure. We take the wave function of a nucleus to be a single Slater determinant of nucleonic one-particle states. These one-particle states are chosen to be eigenfunctions of a three-dimensional harmonic oscillator. We assume the nucleus to have axial symmetry, so it is convenient to separate the axial coordinate from the other two (in-plane) coordinates. In this $(2+1)$-D coordinate system, the nucleonic one-particle wave functions become

$$\psi_{nl,m}(\mathbf{r}) = \varphi_{nl}(\boldsymbol{\rho})\chi_m(z). \tag{32}$$

Here $\varphi_{nl}(\boldsymbol{\rho})$ are normalized eigenfunctions of a 2-D oscillator in the plane perpendicular to the intrinsic axis. They are described by the quantum numbers n and l referring to the state's energy and orbital angular momentum, respectively. The normalized eigenstates of a 1-D oscillator $\chi_m(z)$ are labeled with the energy quantum number m. Our model interaction, Eq. (1), has no spin variables. Therefore the spatial parts of the wave functions do not depend on spin. Constructed in this fashion, the one-particle wave functions depend on two parameters: the imputed ''spring constants'' of the one- and two-dimensional oscillators, $\hbar\omega_z$ and $\hbar\omega_\perp$. A convenient parameter choice is

$$\eta \equiv \frac{\mu\omega_z}{\hbar} \ \text{ and } \ \xi \equiv \frac{\mu\omega_\perp}{\hbar}. \tag{33}$$

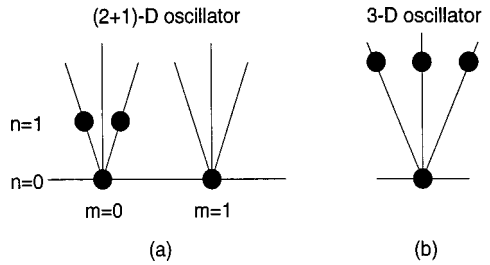

FIG. 2. The dot diagram of the ground state of ^{16}O in $(2+1)$-D (a) and 3-D (b) models. The two diagrams are equivalent when the two ''spring constants'' in the $(2+1)$-D model are equal.

In even-even, $N=Z$ nuclei (including nuclear matter), we take each spatial orbital (*nl, m*) to be occupied by four nucleons (proton, spin up and down, neutron, spin up and down). If we specify the set of all such occupied orbitals (*nl, m*) in a nucleus with *A* nucleons, we have defined a ''nuclear configuration.'' The binding energy of this configuration is calculated by minimizing the expectation value of the potential (1) plus the kinetic energy operator with respect to the variational parameters η and ξ of the Slater determinant $\psi_{\eta,\xi}(\mathbf{r}_1,\ldots,\mathbf{r}_A)$. The configuration with the largest binding energy will of course be the ground state while the other configurations will describe a subset of possible excited states.

It is convenient to visualize these nuclear configurations by using ''dot diagrams.'' We will call ''a dot'' a set of quantum numbers (*nl, m*). A fully occupied orbital containing two (spin-up and spin-down) protons and two neutrons is referred to as ''a full dot.'' An unoccupied orbital is called ''an empty dot.'' The nuclear configurations we entertain are represented by a certain number of full dots arranged in the following order. We place vertical ''trees'' of dots along the horizontal direction from left to right. All dots in a tree have the same quantum number *m*. The first tree corresponds to $m=0$, the second tree to $m=1$, and so on. The bottom of a tree contains a dot with $n=0$ and $l=0$. On going up the tree, the value of *n* is incremented by one. For even *n*, the value of *l* remains 0 on the vertical line of the tree, and changes by -2 or $+2$ to the left or right of the vertical, respectively. For odd *n*, all *l*'s are odd, so there is no dot on the vertical line. Each tree represents a two-dimensional oscillator with a given quantum number *m*. Owing to the condition $-n\leqslant l \leqslant n$, $\Delta l=2$, the dots arrange themselves in a treelike regular pattern. The number of trees in a diagram we call ''modality'' and denote it by *M*.

To illustrate the foregoing description, let us consider the dot diagram of the ground state of ^{16}O in Fig. 2. This diagram has modality $M=2$. The first tree has four nucleons in the state (0, 0, 0), (bottom dot), four nucleons in the state (1, -1, 0), (upper left dot), and four nucleons in the state (1, 1, 0), (upper right dot). The remaining four nucleons belong to the second tree and are in the state (0, 0, 1). As it turns out (not unexpectedly), the two spring parameters, η and ξ, acquire equal values upon minimization. (This will be the case for all closed-shell nuclei: ^{4}He, ^{16}O, ^{40}Ca, ^{80}Zr.) It follows that ^{16}O has a spherically symmetric shape. In this case, the ground-state configuration could be represented by a 3-D dot diagram, as in Fig. 2(b), with the upper middle dot equivalent to the second tree dot of Fig. 2(a). The $(2+1)$-D dot diagrams can be viewed as a generalization of the 3-D dot diagrams, the latter being applicable to spherically symmetric nuclei only.

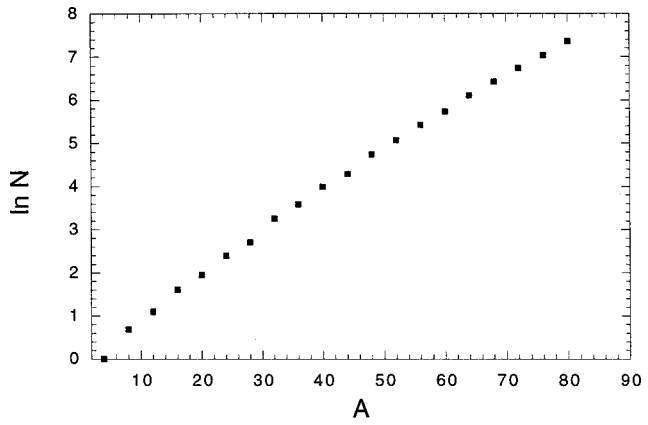

FIG. 3. The number of minimized configurations *N* as a function of the atomic number *A* on a logarithmic scale (to the base *e*).

Without any *a priori* knowledge about which configuration corresponds to a ground state and relative energies of different configurations, all reasonably possible configurations must be considered. This involves calculating and minimizing the energy for each configuration. Due to the simple structure of our potential, we are able to entertain a very large number of configurations. Nevertheless, special care has to be taken to avoid redundant or unrealistic configurations. For ^{4}He the dot diagram is trivial. For ^{3}Be there are two possible dot diagrams to consider. By ^{80}Zr, with some reasonable constraints on the number of possible diagrams, we have minimized 1575 different configurations (see Fig. 3). The algorithm of the calculations is as follows.

First, we choose a nucleus with $A=2N=2Z$ and decide on its maximum possible modality $M_{\max}$. Clearly, $M_{\max}$ cannot exceed $A/4$. On the other hand, calculations show that for the largest nucleus studied, ^{80}Zr (which has only 20 full dots), the number of trees, or modality, can be safely chosen not to exceed seven. All other configurations would represent highly excited shapes. In every tree, the dots are filled from the bottom up. If the top level in a tree is not entirely full, all possible permutations of full dots in this level are considered. However, one should recognize that the states (*n, l, m*) and $(n,-l,m)$ are degenerate. In addition, two other restrictions are applied:

(i) Configurations with the last three trees occupied by dots with $n=0$, $l=0$ only are highly excited, so they are not considered.

(ii) For given *n* and *l*, full dots will first occupy the tree with the smallest available *m*. Otherwise, the energy of the configuration can be lowered by the permutation $(nl,m) \rightarrow (nl,m-1)$;

Examples of these rules are shown in Figs. 4(a) and 4(b), which are configurations ignored by constraints (i) and (ii) for ^{64}Ge. With these restrictions in mind and the fact that the

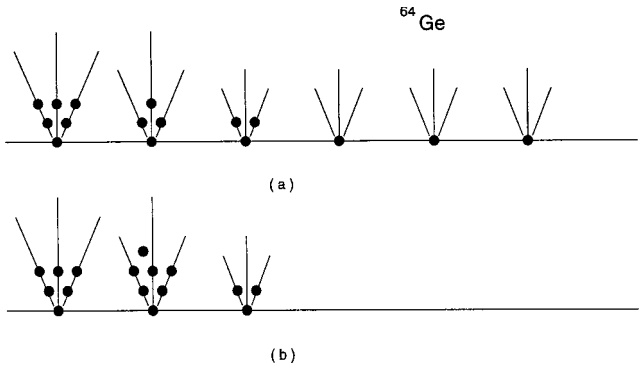

FIG. 4. Two examples of diagrams excluded by our selection rules (i) and (ii) for ^{64}Ge.

states (n, l, m) and $(n,-l,m)$ are degenerate, the total available ''dot space'' for $4 \leqslant A \leqslant 80$ includes 34 different dots $(l \leqslant 0)$, as shown in Fig. 5.

For a given A and $M_{\max}$, we generate all possible configurations of dots subject to the above constraints. For each configuration, we calculate its kinetic energy and interaction energy. The expression for the kinetic energy is readily obtained by enumerating the occupied states of a $(2+1)$-D harmonic oscillator. The interaction energy is the sum of all pairwise nuclear interactions that can be conveniently divided into ''self-dot'' interactions (interactions between two nucleons belonging to the same dot) and ''cross-dot'' interactions (for any two nucleons belonging to two different dots). An important simplification arises from the fact that we can separate the one- and two-dimensional parts of the interaction. The corresponding 1-D and 2-D integrals are calculated separately (see the Appendix) and tabulated numerically for the δ-function repulsion, or as analytical functions of the two parameters, η and ξ, for the finite-range attraction (the range parameter s enters these functions explicitly). The exchange part of the entire repulsion energy and the self-dot portion of the attraction energy is responsible for the factor 3/4 in front of the direct term (the two nucleons have the same orbitals in both these cases). The attractive-energy exchange term for the cross-dot interactions is calculated in the statistical approximation, described above.

Minimization in η and ξ (which are, of course, the same for all orbitals) gives the binding energy of each configuration and is performed numerically using a simple Zeidel-type algorithm. This algorithm, generalized for a large number of variables (up to $\sim$100), will be discussed in more detail in Ref. [16].

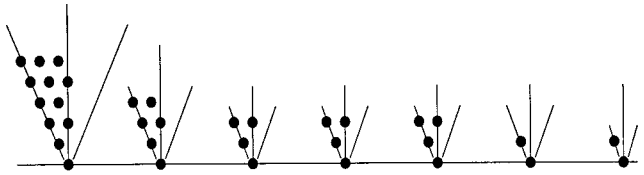

FIG. 5. The set of dots having $l \leqslant 0$ needed for even-even, $N=Z$ nuclei up to ^{80}Zr. The dots on the right-hand side of the trees have been omitted because they generate the same integrals as their partners on the left.

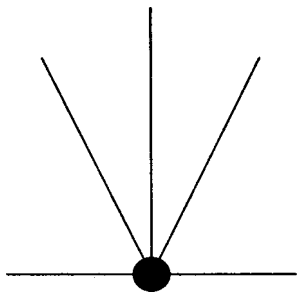

FIG. 6. The dot diagram of ^{4}He.

It is important to emphasize here that we study a small class of all possible nuclear excitations, namely, the ''dot'' excitations, by which a full dot, or two protons and two neutrons, simultaneously go into a higher $(2+1)$-D oscillator orbital. Such transitions are accompanied by significant changes in nuclear shape. Therefore, the excitations studied are, in essence, shape excitations, and the classification of excited states given below is a classification of nuclear shape excitations.

IV. RESULTS

In this section, we present the results of our calculations for even-even, light symmetric nuclei: their ground states, a few excited states, corresponding binding energies and deformations. We assume ellipsoidal deformations characterized by the deformation parameter β:

$$R(\theta,\phi)=R_{\rm av}[1+\beta Y_{20}(\theta,\phi)] \quad \text{or} \quad \beta=\sqrt{\frac{4\pi}{5}}\left(\frac{\langle z^2\rangle^{1/2}}{R_{\rm av}}-1\right). \tag{34}$$

Here $R_{\rm av}$ is the geometric average of the three rms radii in the x, y, and z directions (two of them being equal):

$$R_{\rm av}=(\langle z^2\rangle^{1/2}\langle x^2\rangle)^{1/3}, \quad \langle x^2\rangle=\tfrac{1}{2}\langle \rho^2\rangle. \tag{35}$$

The rms radii for a nucleus are calculated as ''dot averages'' over a given configuration with N (full) dots:

$$\langle z^2\rangle=\frac{1}{N}\sum_\nu \langle z^2\rangle_\nu, \quad \langle \rho^2\rangle=\frac{1}{N}\sum_\nu \langle \rho^2\rangle_\nu, \quad \nu=\{n,l,m\}. \tag{36}$$

In deciding on the ground state of a nucleus, due to the degeneracy of the states (n, l, m) and $(n,-l,m)$, an additional condition that the resultant configuration has the smallest possible total orbital momentum, L, was imposed. Identical configurations with higher L would exhibit a larger

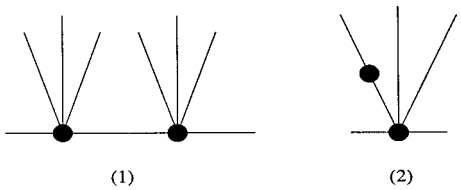

FIG. 7. The dot diagrams of ^{8}Be.

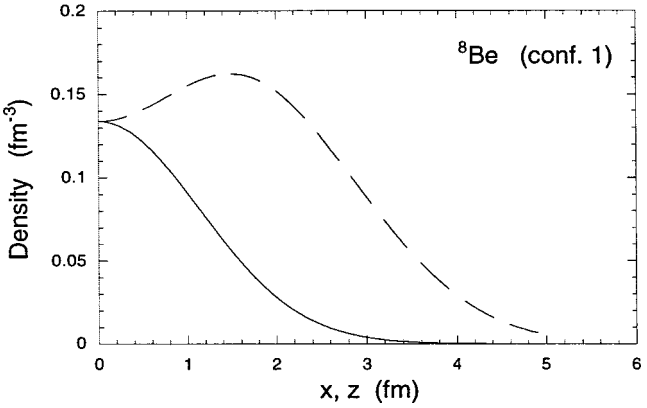

FIG. 8. Nucleon density profile for the ground state of ^{8}Be. Here, and in the subsequent density profile pictures, the solid line corresponds to the radial density distribution ($z=0$), and the dashed line corresponds to the density distribution along the intrinsic z axis.

value of the orbital momentum component associated with rotation around the axis perpendicular to the intrinsic z axis. (L is, of course, the projection of the total angular momentum on the z axis.)

^{4}He. The dot diagram (Fig. 6) is trivial. Both oscillator parameters come out to be equal: $\hbar\omega_z=\hbar\omega_\perp=17.43$ MeV, making the nucleus spherically symmetric. The rms radius is 1.89 fm, slightly larger than the experimental value of 1.61 fm. The binding energy (neglecting, of course, the Coulomb interaction) is, $B=7.27$ MeV per nucleon.

^{8}Be. Two possible dot diagrams are shown in Fig. 7. Configuration 1 (the ground state) has $B=5.49$, $\hbar\omega_z=9.43$, $\hbar\omega_\perp=16.21$ MeV, $\beta=0.81$. Observe that the ground state has a large prolate deformation. The corresponding density profile (Fig. 8) makes it easy to explain the experimental fact that ^{8}Be is unstable and breaks up into two α particles. The first excited-dot diagram (configuration 2) is oblate with $B=3.94$, $\hbar\omega_z=16.00$, $\hbar\omega_\perp=12.06$ MeV, and $\beta=-0.32$.

^{12}C. The dot diagrams are shown in Fig. 9, and the corresponding data are given in Table I. The ground state has an oblate deformation. The nearest shape excitation has an excitation energy of about 1 MeV per nucleon. Configuration 3 adds another 1 MeV/nucleon in excitation energy and is, as expected from the dot diagram, highly deformed along the z axis. The nuclear density profile for the ground state is shown in Fig. 10.

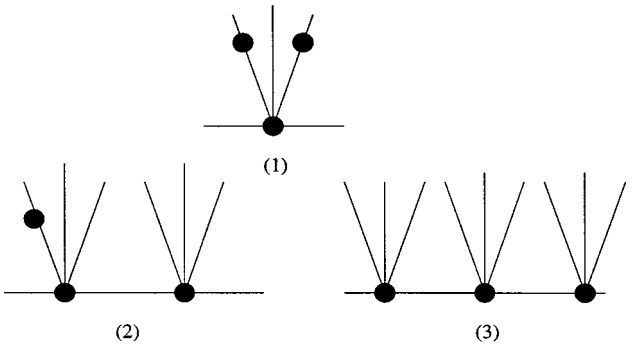

FIG. 9. The dot diagrams of ^{12}C.

TABLE I. Minimization results for ^{12}C.

Configuration	B (MeV)	$\hbar\omega_z$ (MeV)	$\hbar\omega_\perp$ (MeV)	β
1	6.60	17.10	11.98	−0.40
2	5.61	11.88	14.19	0.23
3	4.95	6.38	15.98	1.52

^{16}O. This is a closed-shell nucleus. The binding energy of the ground state is close to the experimental value of 8.8 MeV/nucleon and the rms radius is slightly smaller than the experimental one (2.58 vs 2.67 fm). The ground state is spherically symmetric with a nucleon density distribution as shown in Fig. 11. An interesting feature here is the almost identical binding energies of configurations 2 and 3, in view of their disparate deformations, as shown in Fig. 12. Another feature is the energy difference between configuration 2 and configuration 4. The two have identical sets of energy quantum numbers, n and m. The higher binding energy for configuration 2 can be explained by larger overlap of the orbital (2, 0, 0) with the rest of the orbitals compared with that of the orbital (2, ±2, 0) of configuration 4. Such splitting occurs frequently. The dot diagrams are shown in Fig. 13; see also Table II.

^{20}Ne. The ground state has a prolate deformation. The first excited configuration has an oblate deformation. The binding energies of the two states are 0.25 MeV apart, but inclusion of the Coulomb repulsion might enhance this difference as it favors a prolate deformation over an oblate one. See Figs. 14 and 15; see also Table III.

^{24}Mg. Configurations 1, 2, and 3 for ^{24}Mg have essentially the same binding energy. The true ground state would depend on the competition of the Coulomb energy corrections. Configurations 1 and 2 are degenerate and have large opposite deformations that could lead potentially to sharp (backbending) features in the rotational spectrum. See Figs. 16–18; see also Table IV.

^{28}Si. The ground state has an oblate deformation (Fig. 19). The spherically symmetric state (configuration 4) lies 1 MeV/nucleon higher than the ground state and has the same binding energy as the extremely deformed (prolate) state of configuration 5 (Fig. 20). See dot diagrams in Fig. 21, see also Table V.

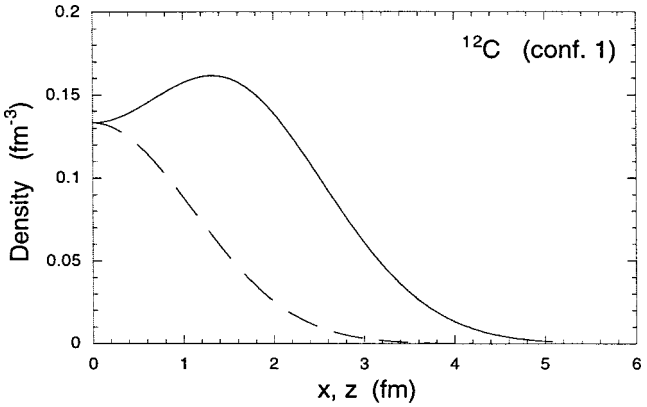

FIG. 10. Nucleon density profile for the ground state of ^{12}C.

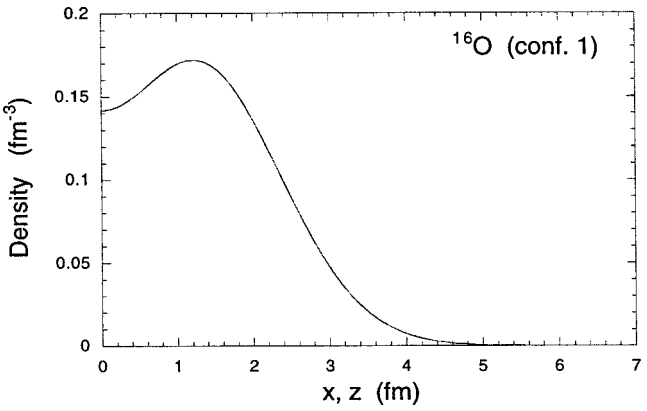

FIG. 11. Nucleon density profile for the ground state of ^{16}O. The nucleus is spherically symmetric.

^{32}S. The first two configurations are essentially degenerate (Figs. 22 and 23), so the true ground state would be determined by the Coulomb contribution to the binding energy. The configurations have opposite deformations that could lead to backbending in the rotational spectrum. See Table VI.

^{36}Ar. The ground state is oblate ($\beta=-0.21$), while the next three excited states are essentially spherically symmetric (Figs. 24 and 25; see also Table VII).

^{40}Ca. This is the case of a closed shell for the $(2+1)$-D oscillator. As expected, the ground state is spherically symmetric (Fig. 26). It is very stable against excitations, and is separated from the first shape excitation by more than 1 MeV/nucleon. The binding energy, by design, is essentially the same as the experimental value of 10.6 MeV/nucleon. Dot diagrams are shown in Fig. 27; see also Table VIII.

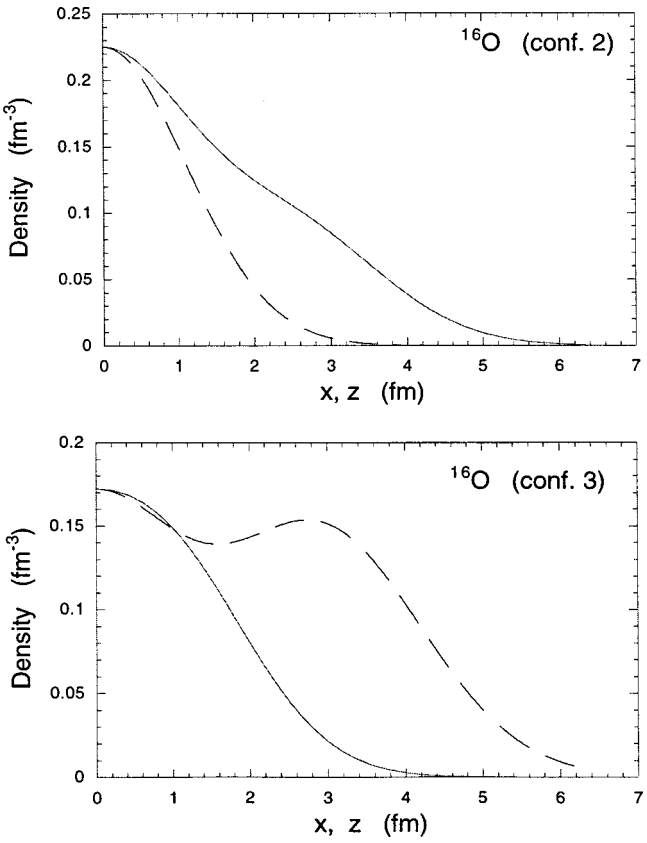

FIG. 12. Nucleon density profile for configurations 2 and 3 of ^{16}O.

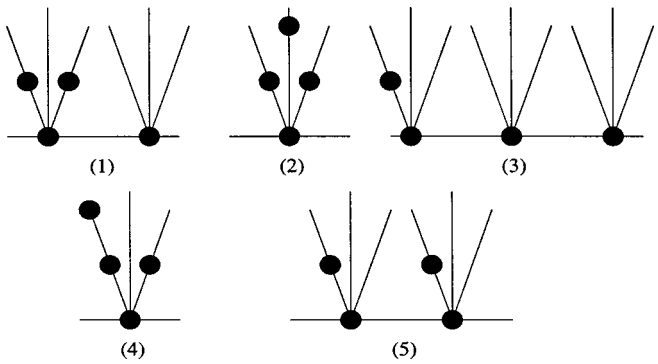

FIG. 13. The dot diagrams of ^{16}O.

^{44}Ti. The ground state has a prolate deformation of $\beta=0.27$. The next two excited shapes are practically symmetric. See Figs. 28 and 29, and Table IX.

^{48}Cr. The ground state has an oblate shape with $\beta=-0.22$. The first excited shape is prolate and is separated by a small amount, $\Delta B=0.13$ MeV/nucleon. See Figs. 30 and 31, and Table X.

^{52}Fe. The ground state has a large prolate deformation, $\beta=0.44$, and is separated from the first shape excitation by a very small gap, $\Delta B=0.09$ MeV/nucleon. This state is oblate with $\beta=-0.29$. See Figs. 32 and 33, and Table XI.

^{56}Ni. The ground state is oblate with $\beta=-0.35$. The first shape excitation is strongly prolate ($\beta=0.68$). The two are separated by $\Delta B=0.21$ MeV/nucleon. See Figs. 34 and 35, and Table XII.

^{60}Zn. The first two configurations are practically identical ($\beta=-0.32$) except for the upper dot in the second tree, which for the ground state prefers orbital (2,0,1) over orbital $(2,\pm2,1)$. The reason for this is the smaller overlap with the rest of the orbitals in the latter case, leading to an energy penalty of 0.16 MeV/nucleon. The next shape excitation lies within 0.2 MeV/nucleon and has a large opposite deformation, $\beta=0.61$. See Figs. 36 and 37, and Table XIII.

^{64}Ge. As in the case of Zn, the first configurations are essentially identical with an oblate deformation of $\beta=-0.30$ (Fig. 38). The interesting feature is the existence of four low-lying shape excitations (with opposite deformations) that range from $\beta=0.16$ to $\beta=0.56$ (see Fig. 39). This may lead to an unusual behavior of its rotational spectrum. See Table XIV and dot diagrams in Figs. 40 and 41.

TABLE II. Minimization results for ^{16}O.

Configuration	B (MeV)	$\hbar\omega_z$ (MeV)	$\hbar\omega_\perp$ (MeV)	β
1	8.59	14.07	14.05	0.00
2	5.58	16.94	10.17	−0.52
3	5.56	8.26	14.85	0.84
4	5.14	16.67	9.88	−0.53
5	3.56	9.48	12.45	0.33

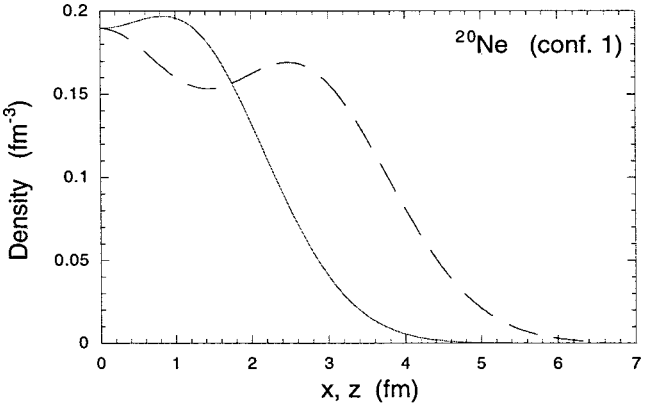

FIG. 14. Nucleon density profile for the ground state of ^{20}Ne.

^{68}Se. In addition to the oblate ground state ($\beta=-0.28$), the nucleus of Se exhibits four essentially degenerate low-lying configurations with quite different shapes ranging from $\beta=0.52$ to $\beta=-0.21$. An interesting rotational spectrum could be expected. See Figs. 42–45, and Table XV.

^{72}Kr. The ground state and the first four-excited configurations are essentially spherically symmetric and nearly degenerate. This is the only case in our study where we had to apply the minimum total angular momentum rule and populate orbital (2,+2,1) instead of orbital (2,−2,1) in the second tree (given the dot distribution of the first tree) in order to obtain an orbital momentum of $L=-1$, instead of $L=-5$. See Figs. 46–48, and Table XVI.

^{76}Sr. The first three configurations are virtually identical in binding energy and deformation (spherically symmetric) (Figs. 49 and 50). This is the case when the excitations are one-dot excitations, as seen from the tree diagrams of Fig. 51. See Table XVII.

^{80}Zr. This is the last closed-shell nucleus studied, just beyond the experimental proton drip line. The closed-shell effects are seen in the sharp peak in the binding energy compared to neighboring nuclei, as well as in the large gap between the ground state and the first shape excitation. The ground state is symmetric, as shown in Fig. 52. The next four configurations are nearly degenerate with small deformations of both signs. See dot diagrams in Figs. 53 and 54 and corresponding data in Table XVIII.

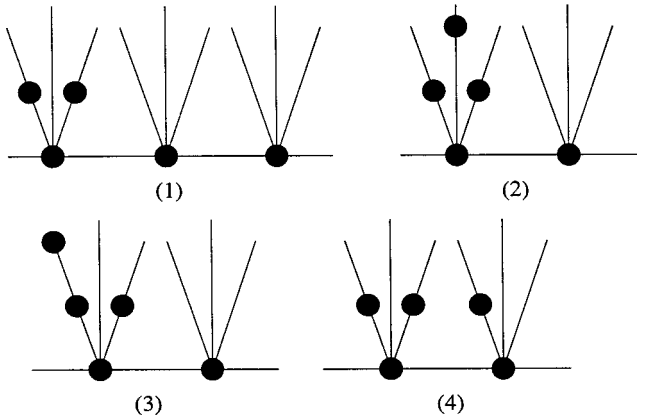

FIG. 15. The dot diagrams of ^{20}Ne.

TABLE III. Minimization results for ^{20}Ne.

Configuration	B (MeV)	$\hbar\omega_z$ (MeV)	$\hbar\omega_\perp$ (MeV)	β
1	8.20	10.15	14.75	0.50
2	7.95	14.90	12.07	−0.23
3	7.14	14.56	11.93	−0.22
4	6.96	11.82	13.07	0.12
5	5.71	16.95	9.27	−0.59

V. DISCUSSION

The calculated binding energies of the ground states for even-even, $N=Z$ nuclei are shown in Fig. 55. They are compared with the Coulomb-corrected experimental values of Möller *et al.* [21]. For ^{68}Se, ^{72}Kr, ^{76}Sr, and ^{80}Zr (as we approach the proton drip line) there is no experimental data available. Therefore, extrapolations from the nearest available experimental data, tabulated in Ref. [21] are used for comparison. A few comments are appropriate here.

The interaction parameters (α, β, and s) were chosen to give exactly the binding energy of ^{4}He and the best possible fit for both ^{16}O and ^{40}Ca. In their ground state, these three nuclei, together with ^{80}Zr, turn out to be closed-shell configurations of the $(2+1)$-D oscillator for modalities $M=1$, 2, 3, and 4, respectively. These four nuclei are the only ones that are spherically symmetric in their ground state, each one being a complete shell of an isotropic 3-D oscillator. They are very stable against deformations, and their binding energies have pronounced peaks, as shown in Fig. 55.

The remainder of the calculated binding energy curve lies below the experimental data. For small A ($8\leqslant A\leqslant 36$) the calculated values are significantly underbound. For large A the calculated values follow the experimental curve rather well. It is reasonable to expect that light nuclei (with their large surface-to-volume ratio) would acquire a larger fraction of their binding energy (compared to heavy nuclei) from many-body corrections beyond the Hartree-Fock approximation, i.e., the correlation energy arising from configuration interaction.

The ground-state shapes (in the ellipsoidal deformation approximation) are summarized in Fig. 56. It is interesting to compare our results with those obtained by Möller *et al.*

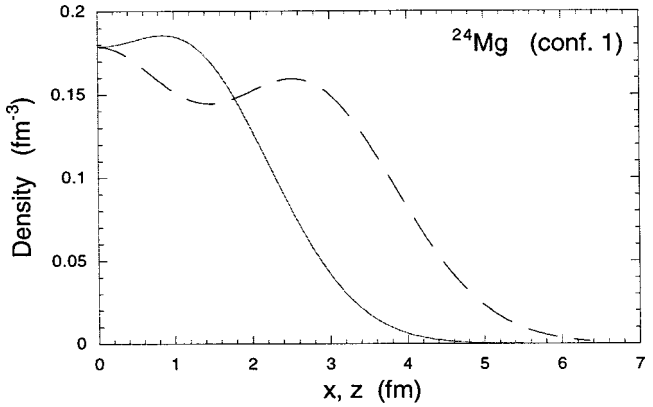

FIG. 16. Nucleon density profile for the ground state of ^{24}Mg.

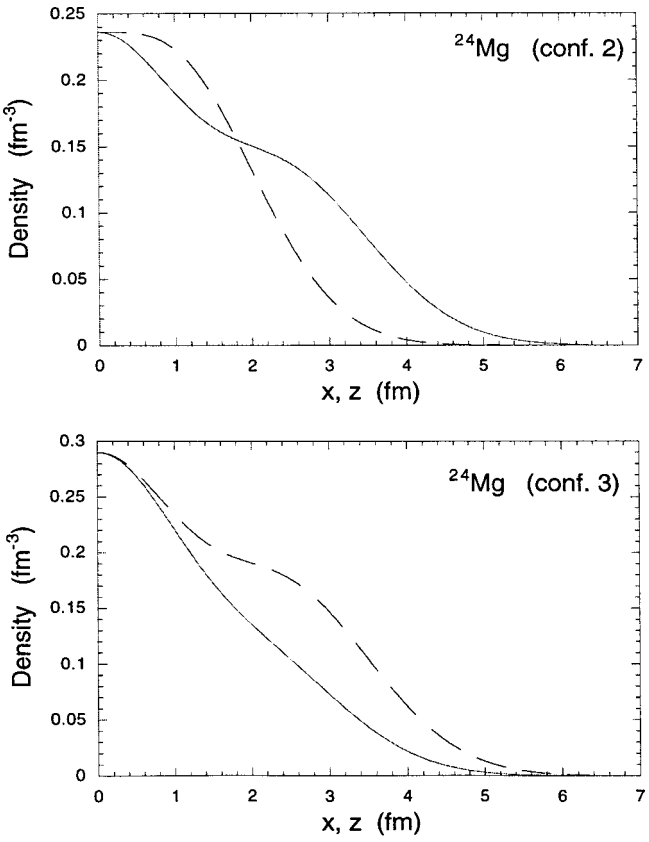

FIG. 17. Nucleon density profile for the first two shape excitations of ^{24}Mg.

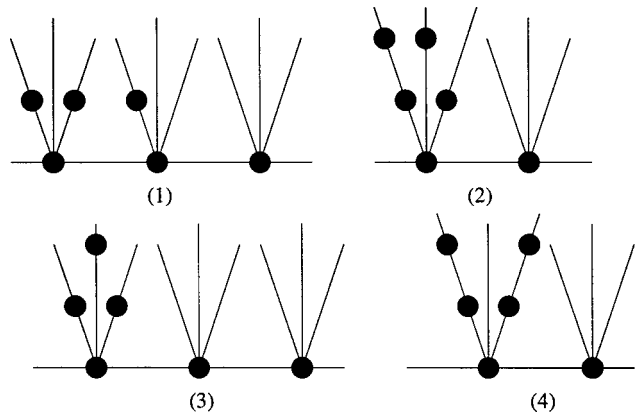

FIG. 18. The dot diagrams of ^{24}Mg.

TABLE IV. Minimization results for ^{24}Mg.

Configuration	B (MeV)	$\hbar\omega_z$ (MeV)	$\hbar\omega_\perp$ (MeV)	β
1	7.93	9.78	14.16	0.49
2	7.92	15.48	11.16	−0.34
3	7.86	11.15	12.92	0.18
4	7.53	15.22	11.00	−0.34
5	7.24	12.98	12.03	−0.09

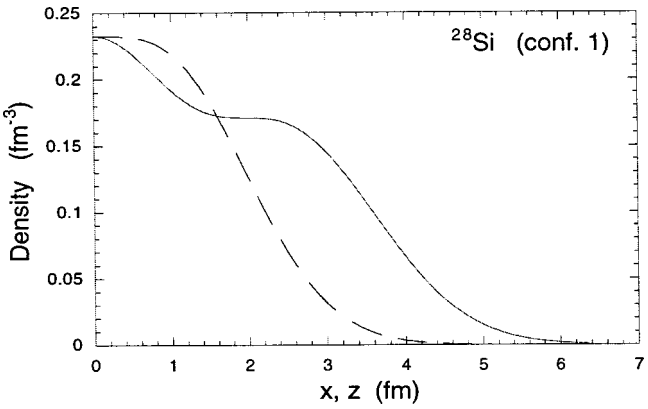

FIG. 19. Nucleon density profile for the ground state of ^{28}Si.

[21]. An important difference is that we ignored the Coulomb repulsion. As expected, for closed-shell nuclei (with the surprising exception of ^{80}Zr), both approaches yield spherically symmetric shapes. We found that all other nuclei are deformed in their ground state.

For light nuclei, where the energy difference between ground and excited states is larger than or comparable to the Coulomb energy, our calculations generally agree with Ref. [21]. However, for A between 32 and 58, spherically symmetric nuclear shapes are predicted in Ref. [21]. Instead, we find that these nuclei are deformed (excepting, of course, ^{40}Ca). Inclusion of the Coulomb energy should enhance pro-

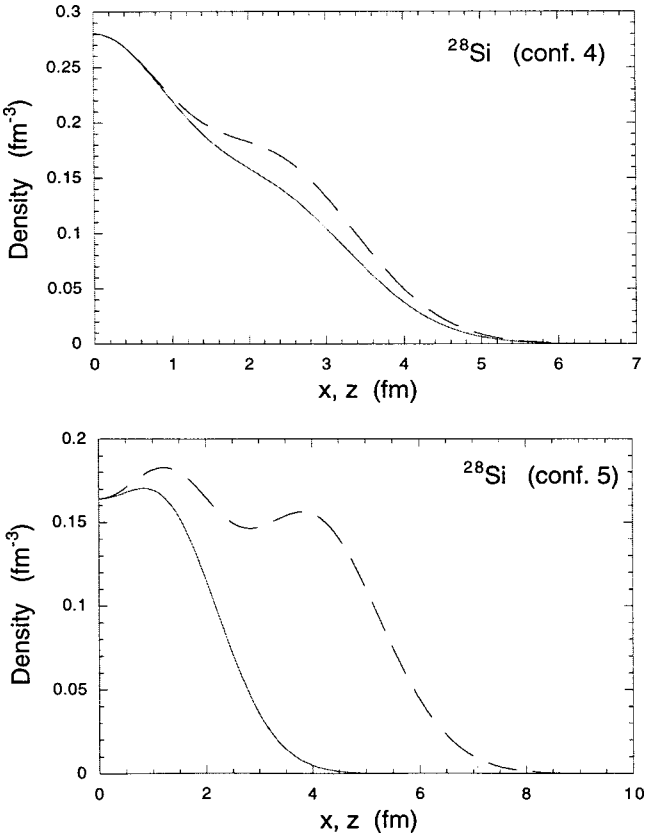

FIG. 20. Density profile for two degenerate excited states of ^{28}Si, configurations 4 and 5.

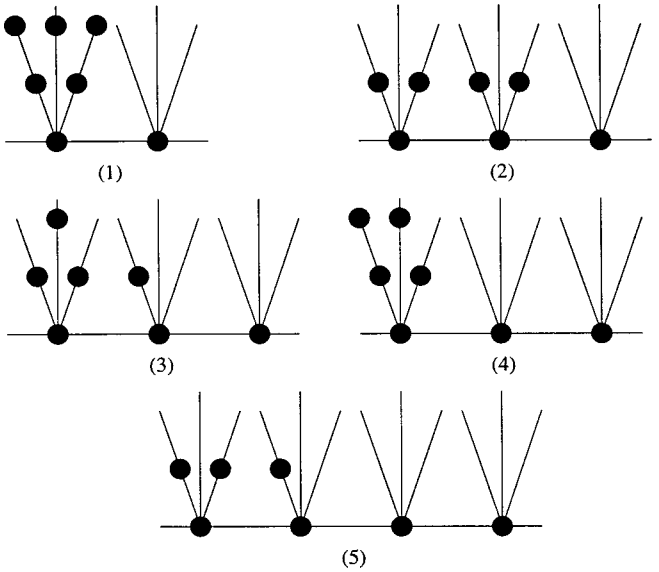

FIG. 21. The dot diagrams of ^{28}Si.

late deformations. Such is likely the case for ^{36}Ar, ^{48}Cr, and ^{56}Ni. Interestingly, two rotational bands in the doubly magic nucleus ^{56}Ni have been recently identified [22]. Including the Coulomb repulsion would likely reverse the sign of the deformations for ^{60}Zn, ^{64}Ge, and ^{68}Se. These nuclei, found to be oblate, have prolate ''excited'' states lying within 0.2 MeV/nucleon of their ground states. The only other nucleus for which the two methods lead to opposite deformations is ^{72}Kr. We found its ground state to be prolate, but its first-excited configuration is oblate (configurations 1 and 2, respectively, in Fig. 47).

It is interesting to consider qualitatively high-spin rotations of light nuclei (about an axis perpendicular to their intrinsic z axis). Such an excitation would lead to a larger deformation in those nuclei already prolate in their ground state, such as ^{20}Ne, ^{24}Mg, etc. For high-spin excitations, nuclei such as ^{28}Si, ^{36}Ar, ^{48}Cr, ^{56}Ni, ^{60}Zn, ^{64}Ge, and ^{68}Se may change their deformations from oblate to prolate, in accordance with their first-excited configuration. The resulting abrupt change in moment of inertia would exhibit a backbending feature in their rotational spectra. This would provide an explanation for the backbending phenomenon alternative to that discussed in Ref. [23] for the case of ^{48}Cr. Transitions involving many dots (often with a change of modality of the dot diagram) could result in rotational states having far longer half-lives than one-particle excitations; i.e., long-lived isomeric states could occur.

TABLE V. Minimization results for ^{24}Si.

Configuration	B (MeV)	$\hbar\omega_z$ (MeV)	$\hbar\omega_\perp$ (MeV)	β
1	8.86	16.11	10.77	−0.42
2	8.56	9.56	13.87	0.49
3	8.15	10.82	12.98	0.23
4	7.85	11.99	12.04	0.00
5	7.84	7.74	14.62	0.92

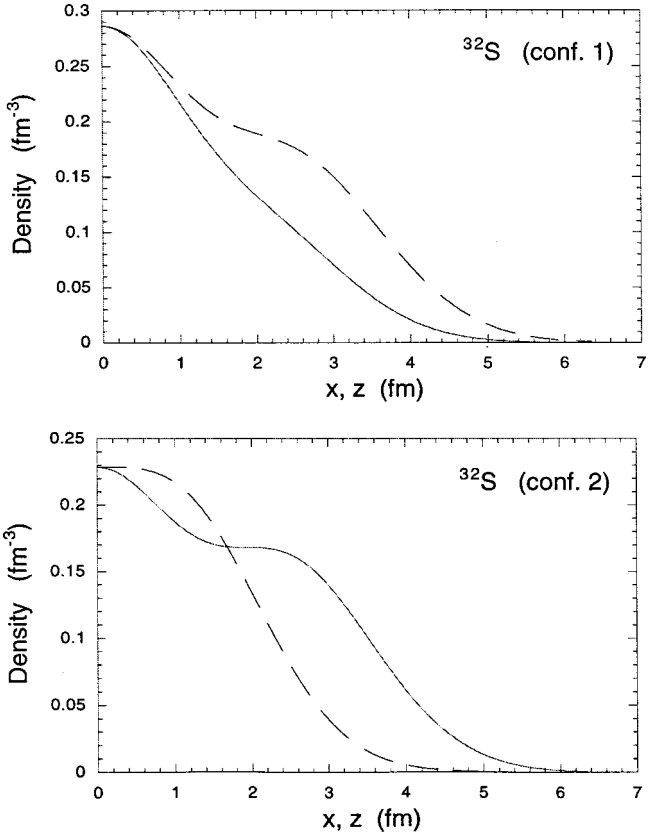

FIG. 22. Nucleon density profile for the ground state and the first collective excited state of ^{32}S.

The dot diagram technique lends itself naturally to the study of exotic molecular states in light nuclei. (See, for example Ref. [24], for a discussion of some experimental results in ^{12}Be.) For example, wave functions of full dots

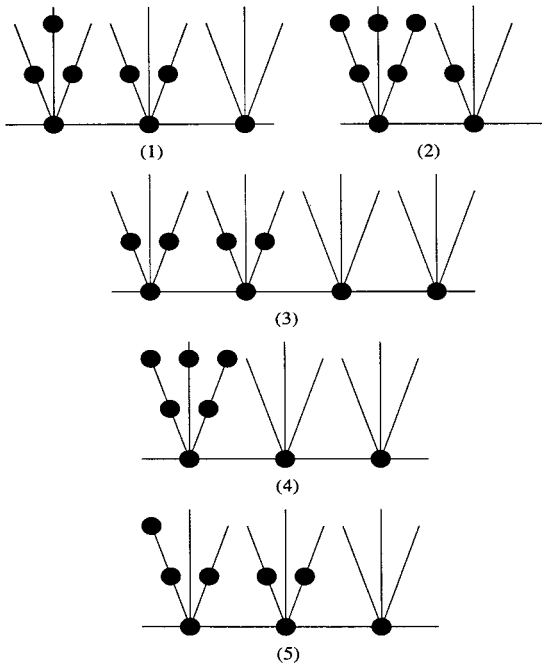

FIG. 23. The dot diagrams of ^{32}S.

TABLE VI. Minimization results for ^{32}S.

Configuration	B (MeV)	$\hbar\omega_z$ (MeV)	$\hbar\omega_\perp$ (MeV)	β
1	9.06	10.57	13.09	0.27
2	9.01	14.70	11.08	−0.30
3	8.79	7.94	14.39	0.85
4	8.71	12.79	11.58	−0.12
5	8.53	10.41	12.88	0.27

with quantum numbers, m and n, at the top level of a tree, can mix with those of empty dots (m',n') from another tree. Such mixing can lead to a density profile with a higher peak-to-trough ratio than that shown for the deformed ground state of ^{8}Be in Fig. 8. Any generalization of the restricted-basis-set Hartree-Fock scheme employed here should be entertained in future work.

Finally, we emphasize once again that we have evaluated only the energies of those configurations for which each orbital basis state is either empty or fully occupied (with four nucleons). Obviously, this subset of all possible configurations is a very small fraction of the totality. One convenient attribute of this subset is that tensor forces and spin-orbit forces do not contribute to the energy. (It should also be noted that a Bardeen-Cooper-Schrieffer pairing energy cannot arise for a single Slater determinant.) If we were to consider even-even nuclei with $N \neq Z$, there would be separate

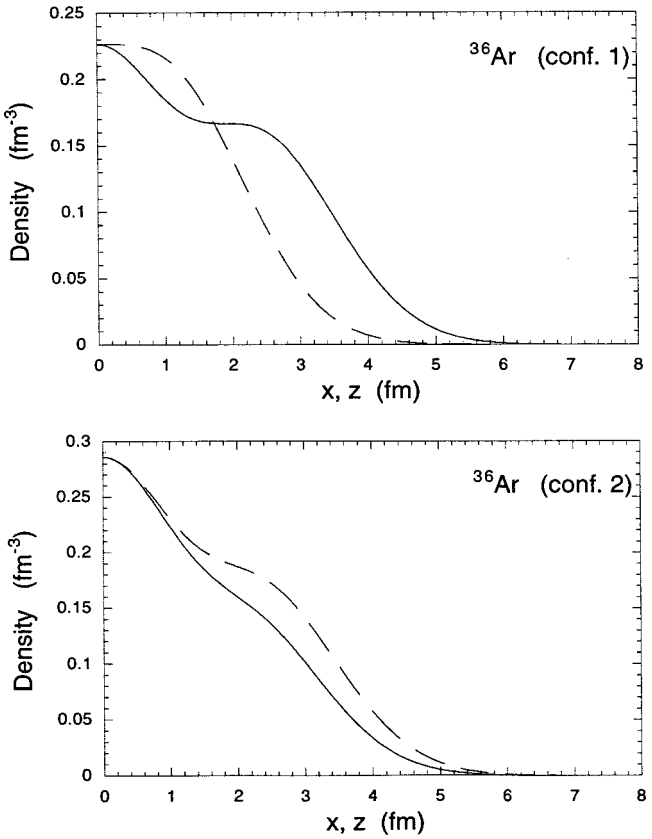

FIG. 24. Nucleon density profile for the ground state and the first collective excited state of ^{36}Ar.

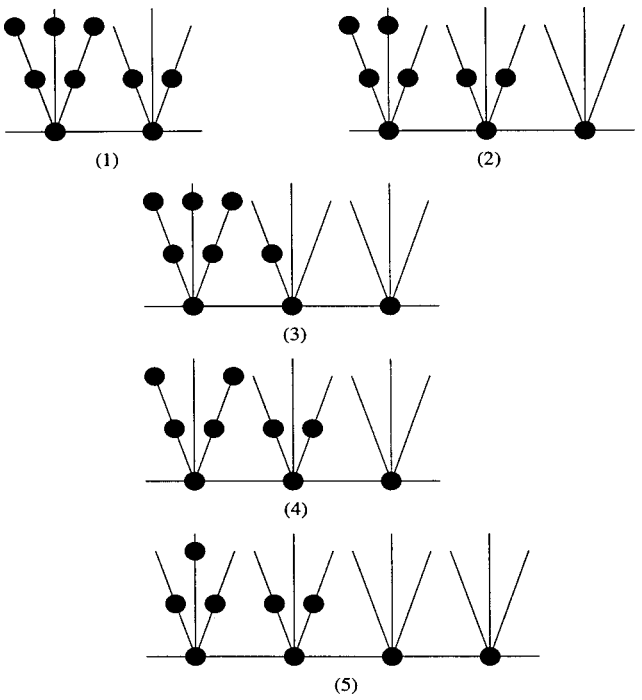

FIG. 25. The dot diagrams of ^{36}Ar.

dot diagrams for neutrons and protons, and $\omega_z^j, \omega_\perp^j$, $j = n,p$, would be distinct wave-function parameters for each species. (The full generality of the HF Hilbert space can occur only if half-filled dots were also admitted, but then spin-orbit and tensor forces would need to be included.)

A perusal of the dot diagrams (and their associated tables in Sec. IV) reveals the large variations of ω_z, $\omega_\perp$, and β from configuration to configuration. This behavior proves that Koopmans' theorem [25] is severely violated in nuclear physics. The reason for this violation is that a one-nucleon orbital energy depends critically on how other orbitals are occupied as well as on ω_z and $\omega_\perp$. (There is no large central potential analogous to the Coulomb potential of an atomic nucleus, which enforces a nominal ordering of electronic energy levels.) The corresponding large variations in density profiles, which reveal the anisotropy of the nuclear radius and, also, the anisotropy of the surface thickness, contribute to the failure of an elementary ordering scheme. Therefore, the collection of dot diagrams cannot be replaced by a simplified model that (implicitly) assumes near validity for Koopmans' theorem.

Of the 20 even-even, $N=Z$ nuclei studied here, ^{4}He, ^{16}O, and ^{40}Ca are surely spherical. Twelve predicted intrinsic de-

TABLE VII. Minimization results for ^{36}Ar.

Configuration	B (MeV)	$\hbar\omega_z$ (MeV)	$\hbar\omega_\perp$ (MeV)	β
1	9.76	13.75	11.35	−0.21
2	9.63	11.42	12.58	0.11
3	9.56	12.50	11.93	−0.05
4	9.31	11.27	12.31	0.11
5	9.18	8.71	13.62	0.59

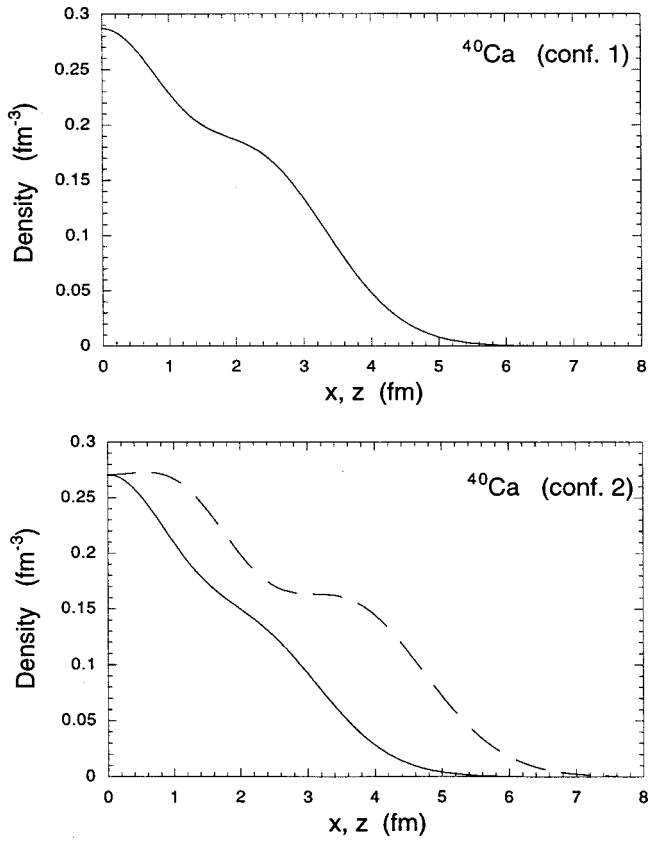

FIG. 26. Nucleon density profile for the ground state (spherically symmetric) and the first shape excitation of ^{40}Co.

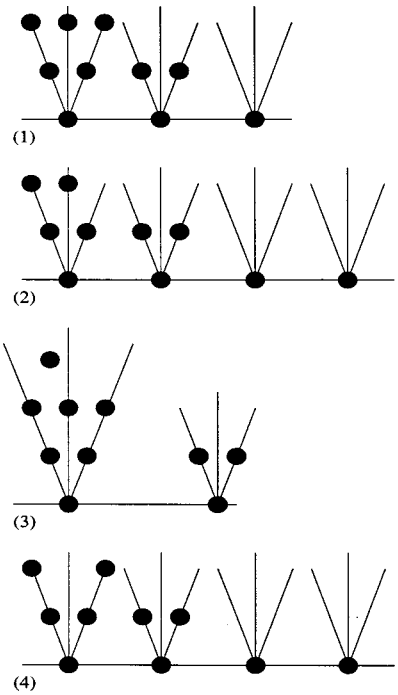

FIG. 27. The dot diagrams of ^{40}Co.

TABLE VIII. Minimization results for ^{40}Ca.

Configuration	B (MeV)	$\hbar\omega_z$ (MeV)	$\hbar\omega_\perp$ (MeV)	β
1	10.76	12.21	12.21	0.00
2	9.61	9.50	13.06	0.41
3	9.50	14.29	10.62	−0.31
4	9.25	9.39	12.86	0.40
5	9.19	13.02	11.02	−0.18

formations of the remaining 17, shown in Fig. 56, from the present work and from the tabulation of Ref. [21], are seriously discrepant. With the advent of new detectors, such as the gammasphere, it may be possible to measure β (including its sign) for some of these contested cases.

Note added. The ground-state deformation of ^{68}Se has recently been measured by Fischer *et al.* [26] and found to be oblate. Resolution of the remaining 11 discrepancies would be of considerable interest.

VI. CONCLUSIONS

In order to study instabilities in symmetric nuclear matter, we have proposed a simple phenomenological nucleon-nucleon potential having three adjustable parameters: attractive strength, attractive range, and repulsive strength (zero range). This potential reproduces four properties of nuclear matter: the binding energy, equilibrium density, compress-

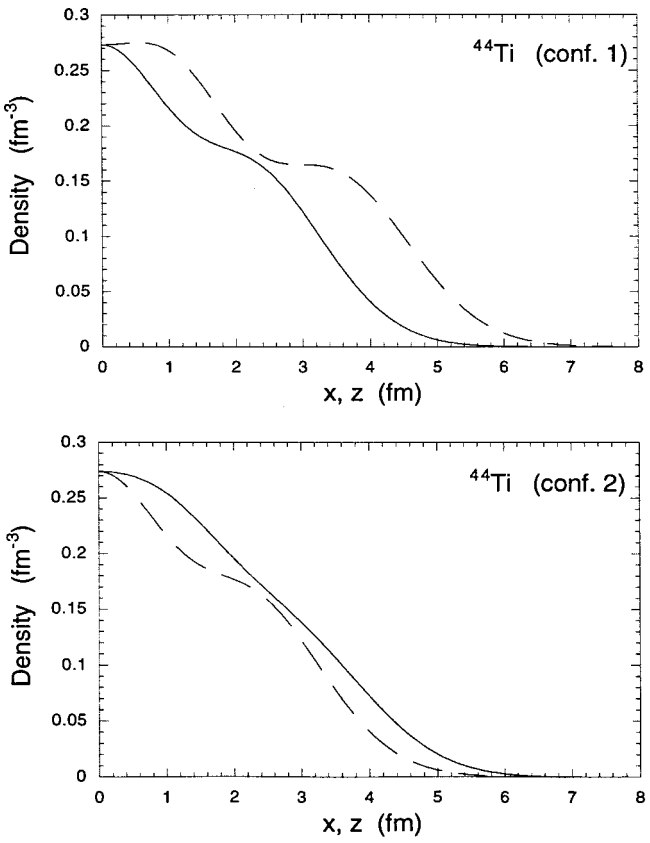

FIG. 28. Nucleon density profile for the ground state and the first shape excitation of ^{44}Ti.

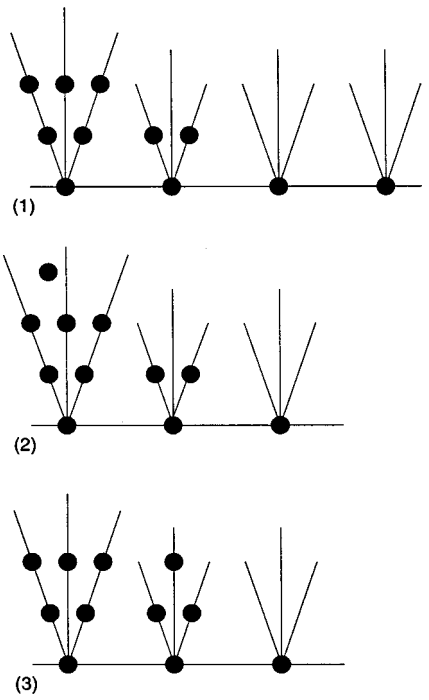

FIG. 29. The dot diagrams of ^{44}Ti.

ibility modulus, and the nucleon effective mass. To prevent spurious ''quasicrystallization'' effects, it is also necessary that the potential reproduces the nuclear part of the binding energies of the even-even, $N=Z$ nuclei: ^{4}He, ^{16}O, and ^{40}Ca.

The dot diagram technique and the statistical approximation for exchange integrals were employed to calculate properties of finite nuclei in a $(2+1)$-D deformed oscillator basis. In this basis, variational Hartree-Fock calculations extending over the configuration space defined by the lowest 55 orbitals were performed. Our attention was focused on spin-zero, isospin-zero nuclei. Therefore, spin-orbit, tensor, and pairing interactions were omitted. In addition, the Coulomb interaction was neglected. Nevertheless, the binding energies and nuclear density profiles of closed-shell, $A=4$, 16 and 40, nuclei were close to the (Coulomb corrected) experimental values. Comparisons with experimental binding energies were made for all even-even, $N=Z$ nuclei up to $A=80$. Large ground-state deformations and exotic nuclear shapes were found for some nuclei. Shape excitations, i.e., shape isomers with diverse deformations, occur frequently. (See Tables I–XVIII.) This phenomenon is well known [27]. We believe that the nucleon-nucleon potential developed here is appropriate for investigating collective instabilities of nuclear matter [16].

TABLE IX. Minimization results for ^{44}Ti.

Configuration	B (MeV)	$\hbar\omega_z$ (MeV)	$\hbar\omega_\perp$ (MeV)	β
1	10.57	10.22	12.70	0.27
2	10.45	12.75	11.40	−0.12
3	10.09	11.68	11.67	0.00

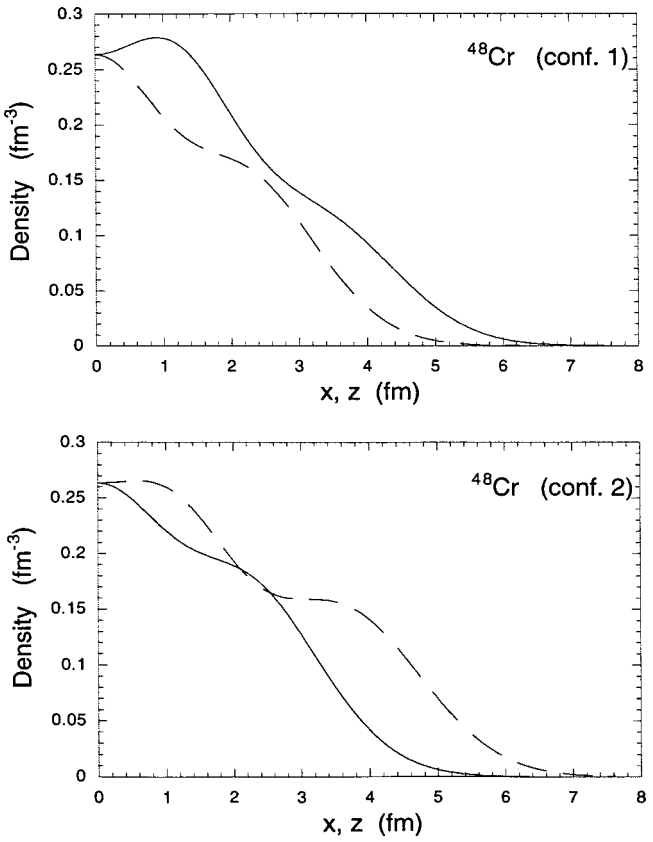

FIG. 30. Nucleon density profile for the ground state and the first shape excitation of ^{48}Cr.

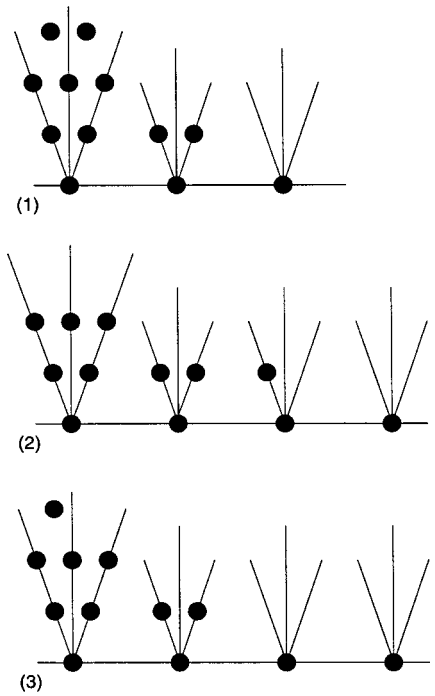

FIG. 31. The dot diagrams of ^{48}Cr.

TABLE X. Minimization results for ^{48}Cr.

Configuration	B (MeV)	$\hbar\omega_z$ (MeV)	$\hbar\omega_\perp$ (MeV)	β
1	10.57	13.24	10.77	−0.22
2	10.44	9.53	12.69	0.36
3	10.25	10.73	11.85	0.12

APPENDIX: EVALUATION OF THE INTERACTION INTEGRALS WITH THE (2+1)-D HARMONIC-OSCILLATOR WAVE FUNCTIONS

In the notation of Eq. (33), the first seven normalized one-dimensional oscillator wave functions are

$$\chi_0(z)=\left(\frac{\eta}{\pi}\right)^{1/4}e^{-(1/2)\eta z^2}$$

$$\chi_1(z)=\left(\frac{\eta}{\pi}\right)^{1/4}\sqrt{2\eta}ze^{-(1/2)\eta z^2}$$

$$\chi_2(z)=\left(\frac{\eta}{\pi}\right)^{1/4}\frac{1}{\sqrt{2}}(2\eta z^2-1)e^{-(1/2)\eta z^2}$$

$$\chi_3(z)=\left(\frac{\eta}{\pi}\right)^{1/4}\frac{1}{\sqrt{3}}(2\eta^{3/2}z^3-3\eta^{1/2}z)e^{-(1/2)\eta z^2}$$

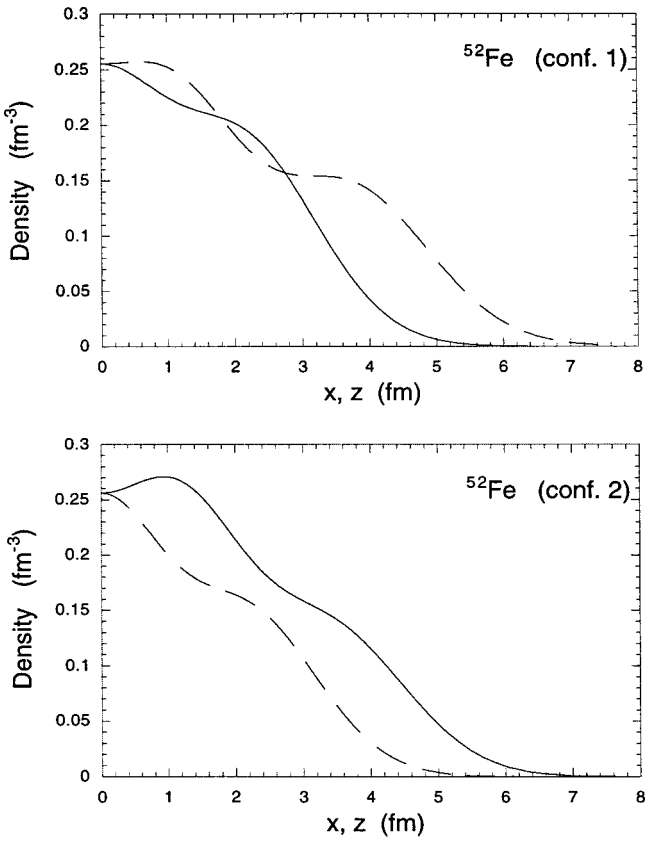

FIG. 32. Nucleon density profile for the ground state and the first shape excitation of ^{52}Fe.

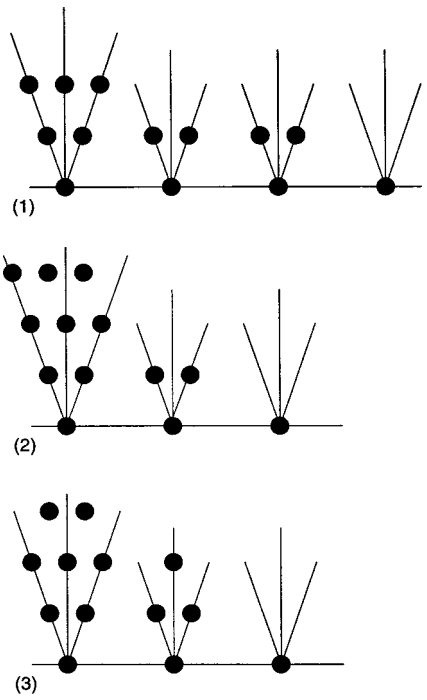

FIG. 33. The dot diagrams of ^{52}Fe.

$$\chi_4(z)=\left(\frac{\eta}{\pi}\right)^{1/4}\frac{1}{\sqrt{24}}(4\eta^2z^4-12\eta z^2+3)e^{-(1/2)\eta z^2}$$

$$\chi_5(z)=\left(\frac{\eta}{\pi}\right)^{1/4}\frac{1}{\sqrt{60}}(4\eta^{5/2}z^5-20\eta^{3/2}z^3+15\eta^{1/2}z)e^{-(1/2)\eta z^2}$$

$$\chi_6(z)=\left(\frac{\eta}{\pi}\right)^{1/4}\frac{1}{\sqrt{720}}(8\eta^3z^6-60\eta^2z^4+90\eta z^2-15)e^{-(1/2)\eta z^2}.$$

The two-dimensional oscillator states for $n=0,...,5$ are

$$\psi_{00}(\rho,\vartheta)=\left(\frac{\xi}{\pi}\right)^{1/2}e^{-(1/2)\xi\rho^2}$$

$$\psi_{1\pm1}(\rho,\vartheta)=\left(\frac{\xi}{\pi}\right)^{1/2}\xi^{1/2}\rho e^{-(1/2)\xi\rho^2}e^{\pm\iota\vartheta}$$

$$\psi_{20}(\rho,\vartheta)=\left(\frac{\xi}{\pi}\right)^{1/2}(1-\xi\rho^2)e^{-(1/2)\xi\rho^2}$$

TABLE XI. Minimization results for ^{52}Fe.

Configuration	B (MeV)	$\hbar\omega_z$ (MeV)	$\hbar\omega_\perp$ (MeV)	β
1	10.65	8.99	12.66	0.44
2	10.56	13.64	10.31	−0.29
3	10.42	12.79	10.60	−0.20

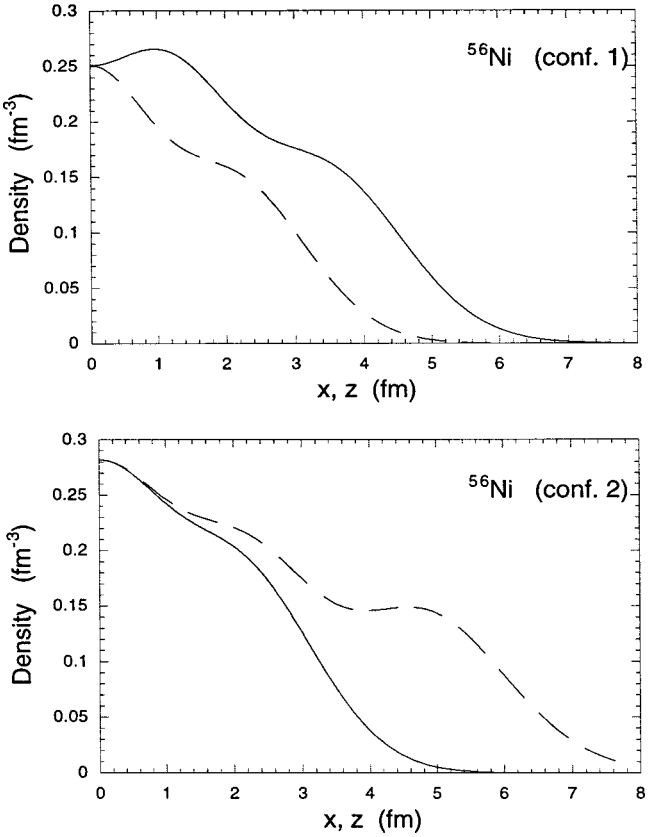

FIG. 34. Nucleon density profile for the ground state and the first shape excitation of ^{56}Ni.

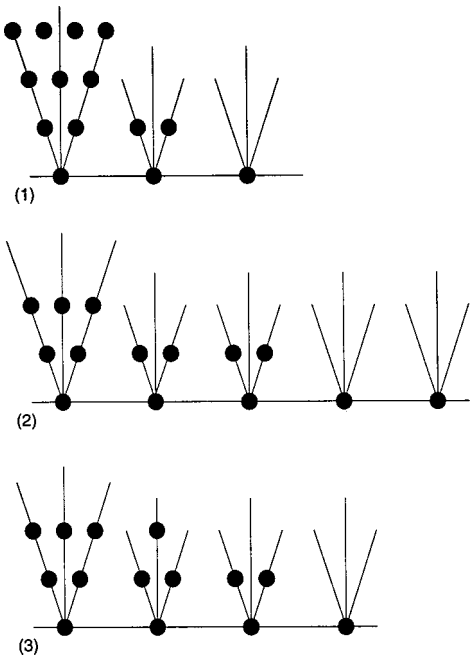

FIG. 35. The dot diagrams of ^{56}Ni.

TABLE XII. Minimization results for ^{56}Ni.

Configuration	B (MeV)	$\hbar\omega_z$ (MeV)	$\hbar\omega_\perp$ (MeV)	β
1	10.90	14.01	9.97	−0.35
2	10.69	7.89	12.98	0.68
3	10.68	9.04	12.34	0.40

$$\psi_{2\pm2}(\rho,\vartheta)=\left(\frac{\xi}{\pi}\right)^{1/2}\frac{1}{\sqrt{2}}\xi\rho^2 e^{-(1/2)\xi\rho^2}e^{\pm 2\iota\vartheta}$$

$$\psi_{3\pm1}(\rho,\vartheta)=\left(\frac{\xi}{\pi}\right)^{1/2}\frac{1}{\sqrt{2}}(2\xi^{1/2}\rho-\xi^{3/2}\rho^3)e^{-(1/2)\xi\rho^2}e^{\pm\iota\vartheta}$$

$$\psi_{3\pm3}(\rho,\vartheta)=\left(\frac{\xi}{\pi}\right)^{1/2}\frac{1}{\sqrt{6}}\xi^{3/2}\rho^3 e^{-(1/2)\xi\rho^2}e^{\pm 3\iota\vartheta}$$

$$\psi_{40}(\rho,\vartheta)=\left(\frac{\xi}{\pi}\right)^{1/2}\frac{1}{\sqrt{4}}(2-4\xi\rho^2+\xi^2\rho^4)e^{-(1/2)\xi\rho^2}$$

$$\psi_{4\pm2}(\rho,\vartheta)=\left(\frac{\xi}{\pi}\right)^{1/2}\frac{1}{\sqrt{6}}(3\xi\rho^2-\xi^2\rho^4)e^{-(1/2)\xi\rho^2}e^{\pm 2\iota\vartheta}$$

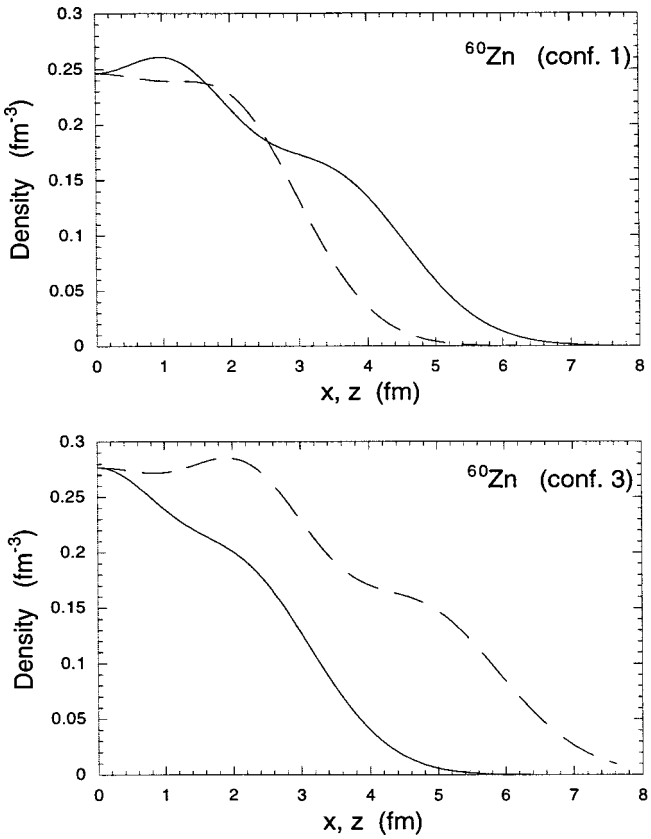

FIG. 36. Nucleon density profile for the ground state (configuration 1) and configuration 3 of ^{60}Zn.

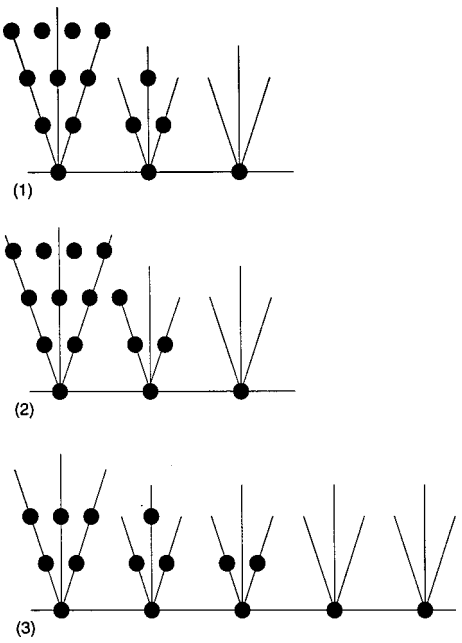

FIG. 37. The dot diagrams of ^{60}Zn.

$$\psi_{4\pm4}(\rho,\vartheta)=\left(\frac{\xi}{\pi}\right)^{1/2}\frac{1}{\sqrt{24}}\xi^2\rho^4 e^{-(1/2)\xi\rho^2}e^{\pm4\iota\vartheta}$$

$$\psi_{5\pm1}(\rho,\vartheta)=\left(\frac{\xi}{\pi}\right)^{1/2}\frac{1}{\sqrt{12}}(6\xi^{1/2}\rho-6\xi^{3/2}\rho^3+\xi^{5/2}\rho^5)e^{-(1/2)\xi\rho^2}e^{\pm\iota\vartheta}$$

$$\psi_{5\pm3}(\rho,\vartheta)=\left(\frac{\xi}{\pi}\right)^{1/2}\frac{1}{\sqrt{24}}(4\xi^{3/2}\rho^3-\xi^{5/2}\rho^5)e^{-(1/2)\xi\rho^2}e^{\pm3\iota\vartheta}$$

$$\psi_{5\pm5}(\rho,\vartheta)=\left(\frac{\xi}{\pi}\right)^{1/2}\frac{1}{\sqrt{120}}\xi^{5/2}\rho^5 e^{-(1/2)\xi\rho^2}e^{\pm5\iota\vartheta}.$$

The interaction potential is given by Eq. (1).

For the integrals involving the repulsive part of the potential, it is convenient to define

$$(nlm,n'l'm')^2_\beta\equiv\int\int d^3r\,d^3r'|\varphi_{nl,m}(\mathbf{r})|^2\times\delta(\mathbf{r}-\mathbf{r}')|\varphi_{n'l',m'}(\mathbf{r}')|^2 \quad \text{(A1)}$$

$$=\int d^3r|\varphi_{nl,m}(\mathbf{r})|^2|\varphi_{n'l',m'}(\mathbf{r})|^2, \quad \text{(A2)}$$

TABLE XIII. Minimization results for ^{60}Zn.

Configuration	B (MeV)	$\hbar\omega_z$ (MeV)	$\hbar\omega_\perp$ (MeV)	β
1	10.99	13.58	9.94	−0.32
2	10.83	13.56	9.92	−0.32
3	10.80	8.00	12.65	0.61

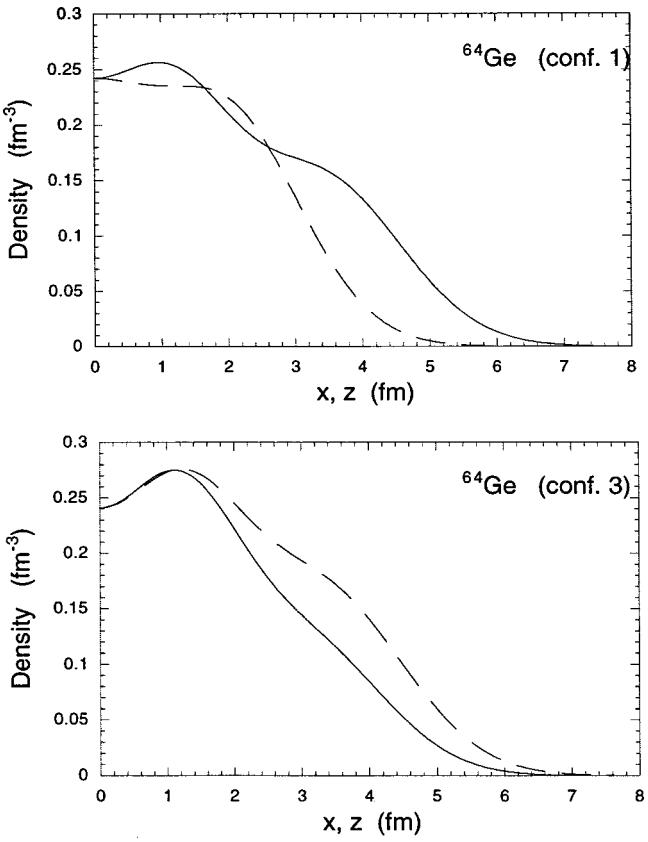

FIG. 38. Nucleon density profile for the ground state of ^{64}Ge.

$$(nlm)^4_\beta\equiv\int d^3r|\varphi_{nl,m}(\mathbf{r})|^4. \quad \text{(A3)}$$

Clearly, the 1-D and 2-D parts of the integrals are separable, and the integrals may be represented as (in the subsequent notation the asterisk stands for any value of quantum numbers n, l, or m, from their entire range, in the order of their appearance)

$$(nlm,n'l'm')^2_\beta=(nl*,n'l'*)^2_\beta(**m,**m')^2_\beta, \quad \text{(A4)}$$

$$(nlm)^4_\beta=(nl*)^4_\beta(**m)^4_\beta, \quad \text{(A5)}$$

with

$$(**m,**m')^2_\beta\equiv\int_{-\infty}^{\infty}dz|\chi_m(z)|^2|\chi_{m'}(z)|^2, \quad \text{(A6)}$$

$$(**m)^4_\beta\equiv\int_{-\infty}^{\infty}dz|\chi_m(z)|^4, \quad \text{(A7)}$$

$$(nl*,n'l'*)^2_\beta\equiv\int d^2\rho|\psi_{nl}(\rho,\vartheta)|^2|\psi_{n'l'}(\rho,\vartheta)|^2, \quad \text{(A8)}$$

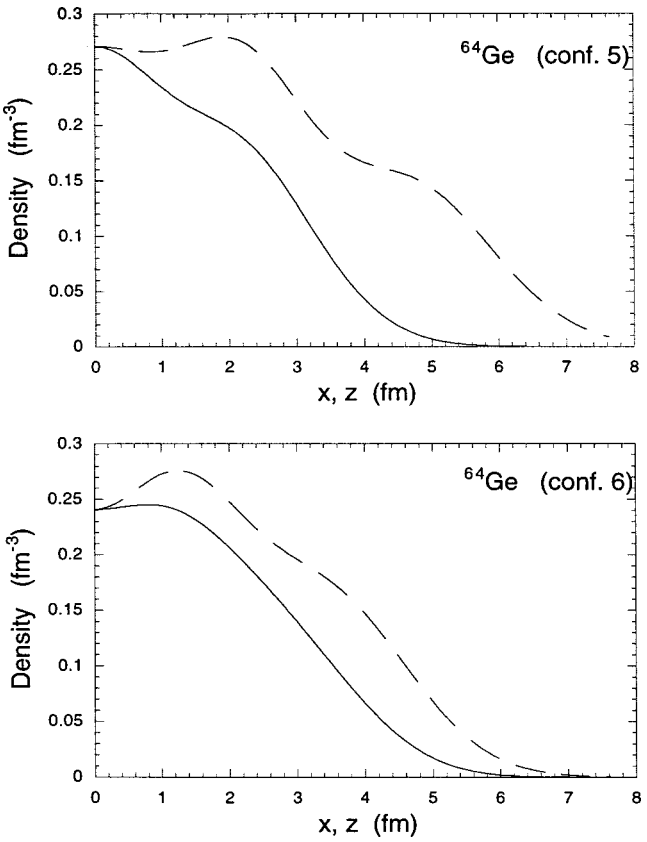

FIG. 39. Nucleon density profile for prolate excited states of ^{64}Ge.

$$(nl*)^4_\beta \equiv \int d^2\rho |\psi_{nl}(\rho,\vartheta)|^4. \tag{A9}$$

Integrals (A6), (A7), (A8), and (A9) are readily calculated, and we present their values in Tables XIX and XX. Summing up all the interacting pairs, we arrive at the final expression for the average repulsive energy. In this expression, in order to simplify the combinatorics, it is convenient to ''expand'' the entire repulsive energy in terms of the 1-D integrals:

$$\langle V_\beta \rangle = \frac{1}{A}\beta\sqrt{\langle T\rangle}\left(\frac{\eta}{2\pi}\right)^{1/2}\left(\frac{\xi}{2\pi}\right)[K_{00}(**0)^4_\beta + K_{01}(**0,**1)^2_\beta + \cdots + K_{0M}(**0,**M)^2_\beta + K_{11}(**1)^4_\beta + \cdots + K_{MM}(**M)^4_\beta]. \tag{A10}$$

TABLE XIV. Minimization results for ^{64}Ge.

Configuration	B (MeV)	$\hbar\omega_z$ (MeV)	$\hbar\omega_\perp$ (MeV)	β
1	11.08	13.20	9.91	−0.30
2	10.98	13.17	9.88	−0.30
3	10.97	9.93	11.37	0.16
4	10.92	9.05	11.80	0.33
5	10.84	8.08	12.32	0.56
6	10.84	9.51	11.62	0.24

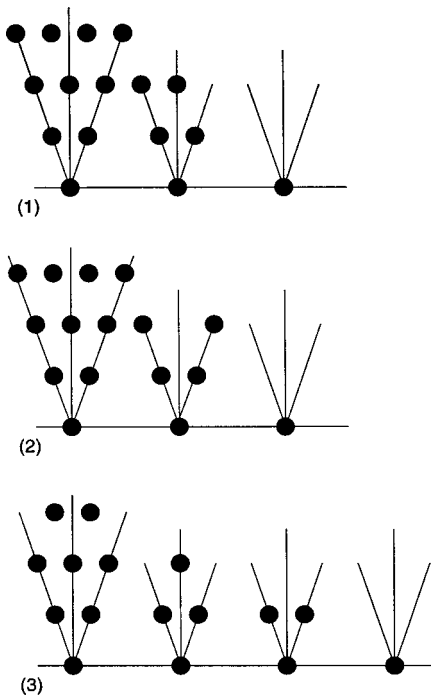

FIG. 40. The first three dot diagrams of ^{64}Ge.

The terms in the brackets are taken to be dimensionless, where K_{ij} are numerical coefficients that include all the 2-D interaction integrals between different dots in the ith and jth trees. If $i=j$, they include the ''self-dot'' interaction, i.e., interaction between nucleons belonging to the same dot. All interacting pairs have the same spatial orbitals owing to the δ function, and the exchange integrals cancel exactly the direct integrals. Therefore, the coefficients K_{ij}, as defined here, do

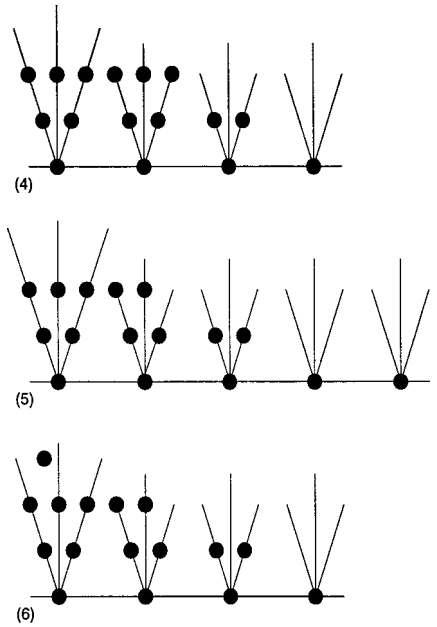

FIG. 41. The next three dot diagrams of ^{64}Ge.

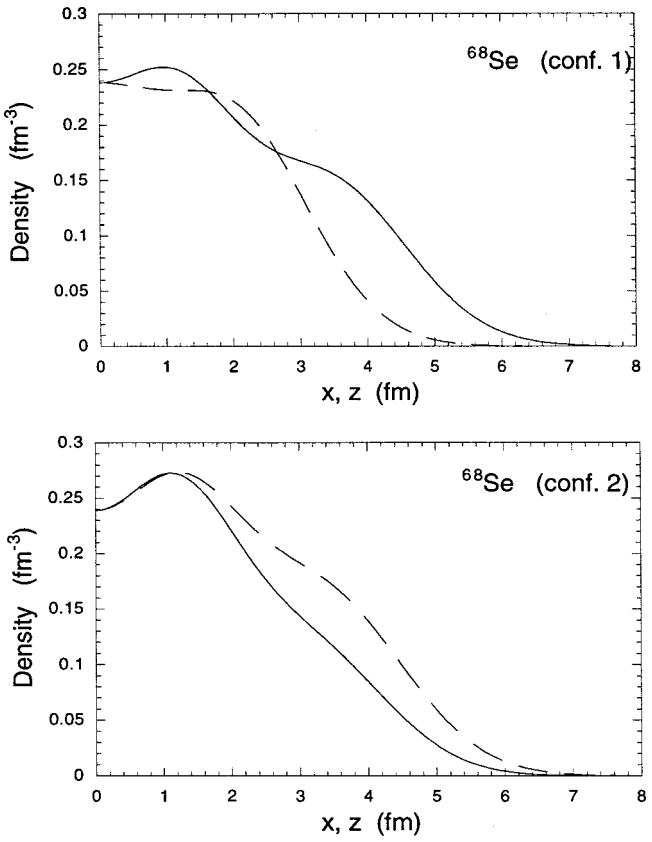

FIG. 42. Nucleon density profile for the ground state and the first shape excitation of ^{68}Se.

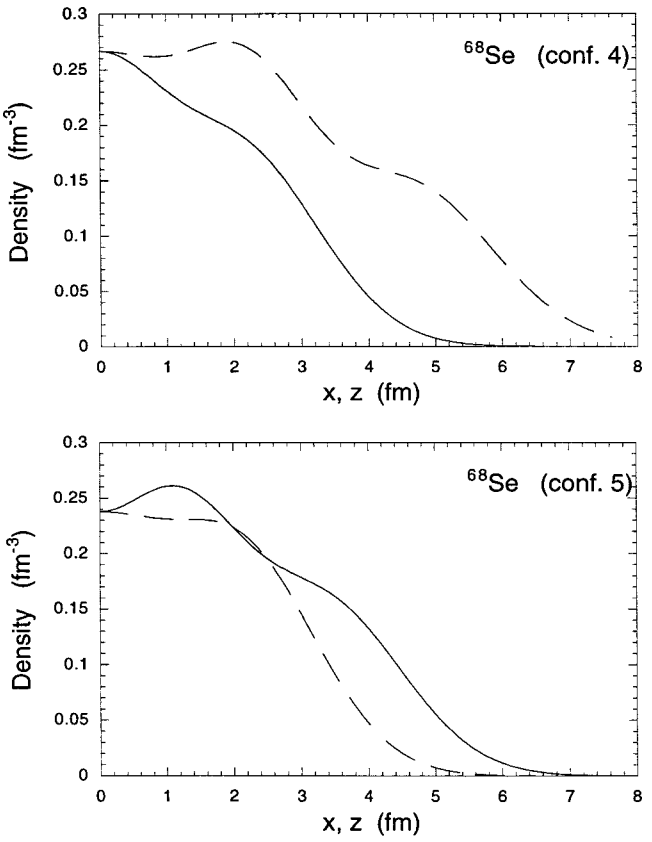

FIG. 43. Nucleon density profile for two degenerate excited states of ^{68}Se. Configuration 4 has a large prolate deformation $\beta = 0.52$ and configuration 5 has an oblate deformation with $\beta = -0.21$.

not include interactions between like particles ($p\uparrow$ with $p\uparrow$, etc.) in both cases, $i=j$ and $i\neq j$, which results in six identical integrals for ''self-dot'' interactions and in 12 identical integrals for interactions between two different dots.

We treat the attractive interaction integrals in a similar way. First, let us show that the one- and two-dimensional integrals are separable. For a pair of nucleons in the states (nl, m) and $(n'l', m')$, respectively, we define

$$(nlm,n'l'm')^2_\alpha \equiv \int\int d^3r\, d^3r' |\varphi_{nl,m}(\mathbf{r})|^2 \times (\mathbf{r}-\mathbf{r}')^2 e^{-(\mathbf{r}-\mathbf{r}')^2/s^2} |\varphi_{n'l',m'}(\mathbf{r}')|^2 \tag{A11}$$

and

$$(nlm)^4_\alpha \equiv \int\int d^3r\, d^3r' |\varphi_{nl,m}(\mathbf{r})|^2 \times (\mathbf{r}-\mathbf{r}')^2 e^{-(\mathbf{r}-\mathbf{r}')^2/s^2} |\varphi_{nl,m}(\mathbf{r}')|^2. \tag{A12}$$

To separate the variables, we notice that

$$(\mathbf{r}-\mathbf{r}')^2 = (\boldsymbol{\rho}-\boldsymbol{\rho}')^2 + (z-z')^2. \tag{A13}$$

Now we may rewrite Eqs. (A11) and (A12) as

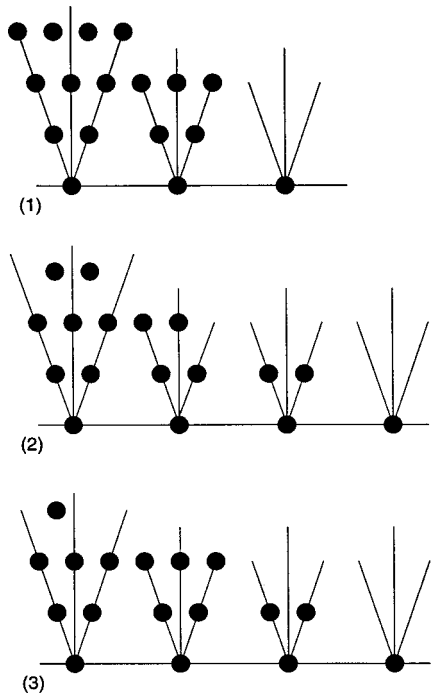

FIG. 44. The first three dot diagrams of ^{68}Se.

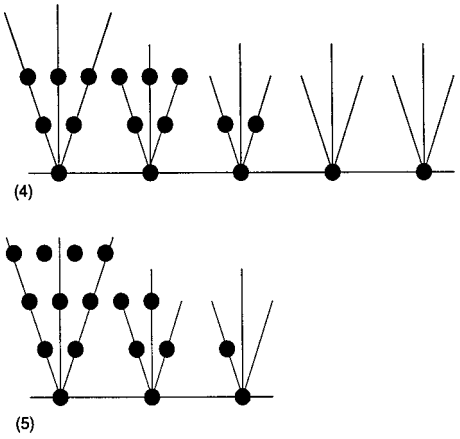

FIG. 45. The next two dot diagrams of ^{68}Se.

TABLE XV. Minimization results for ^{68}Se.

Configuration	B (MeV)	$\hbar\omega_z$ (MeV)	$\hbar\omega_\perp$ (MeV)	β
1	11.34	12.85	9.88	−0.28
2	11.20	9.93	11.27	0.15
3	11.16	9.50	11.47	0.23
4	11.09	8.15	12.07	0.52
5	11.08	12.28	10.09	−0.21

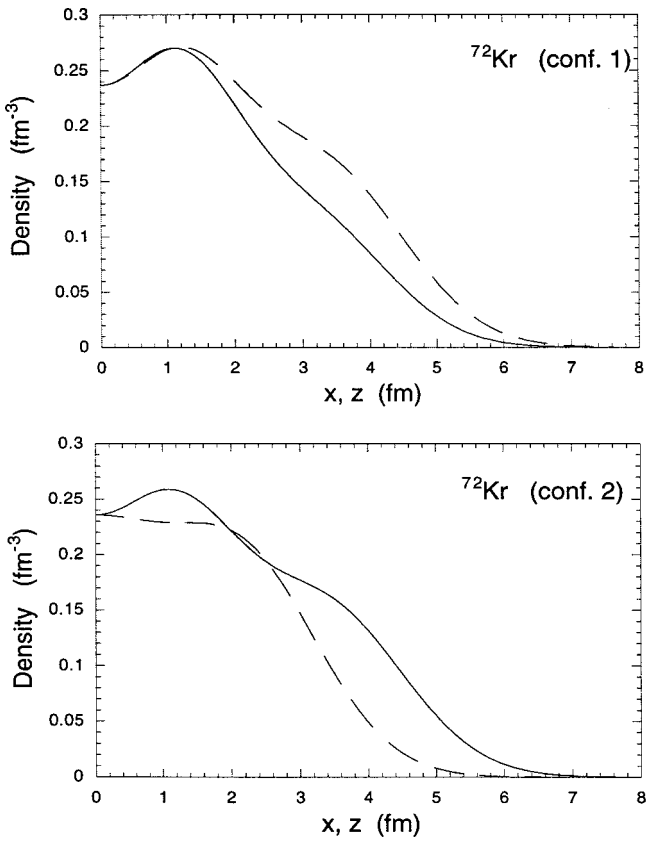

FIG. 46. Nucleon density profile for the ground state and the first shape excitation of ^{72}Kr.

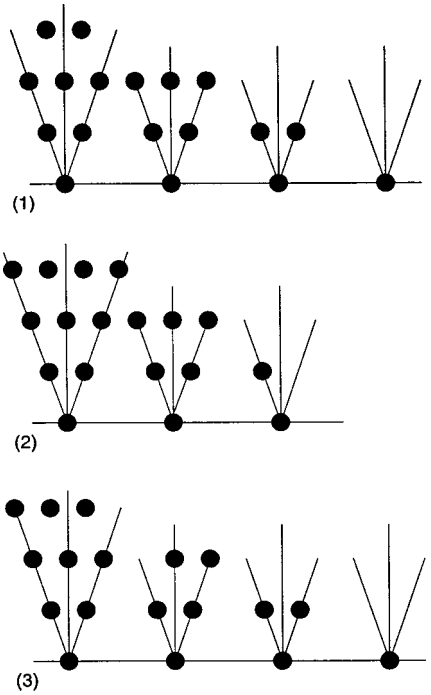

FIG. 47. The first three dot diagrams of ^{72}Kr.

$$(nlm,n'l'm')^2_\alpha=\overline{(nl*,n'l'*)^2_\alpha}(**m,**m')^2_\alpha + (nl*,n'l'*)^2_\alpha\overline{(**m,**m')^2_\alpha} \tag{A14}$$

and

$$(nlm)^4_\alpha=\overline{(nl*)^4_\alpha}(**m)^4_\alpha+(nl*)^4_\alpha\overline{(**m)^4_\alpha}, \tag{A15}$$

where

$$(**m,**m')^2_\alpha\equiv\int_{-\infty}^{\infty}\int_{-\infty}^{\infty}dz\,dz'|\chi_m(z)|^2e^{-(z-z')^2/s^2}\times|\chi_{m'}(z')|^2, \tag{A16}$$

$$(**m)^4_\alpha\equiv(**m,**m)^2_\alpha, \tag{A17}$$

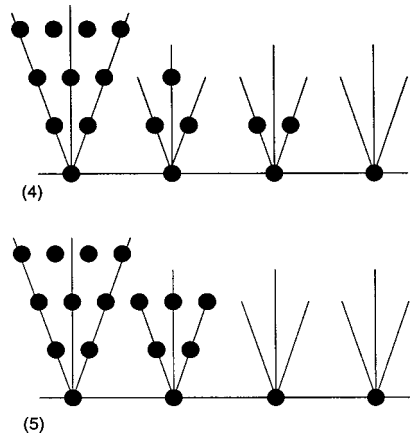

FIG. 48. The next two dot diagrams of ^{72}Kr.

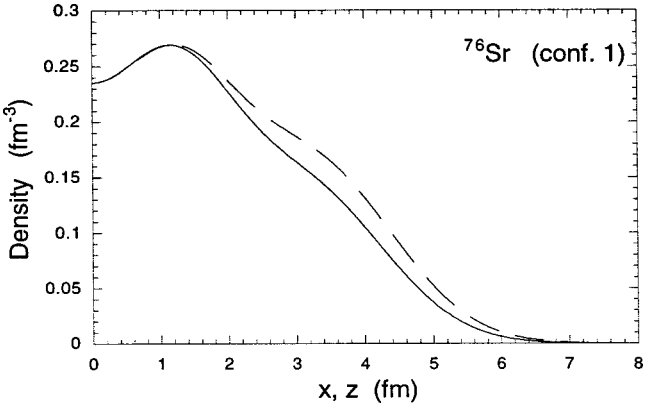

FIG. 49. Nucleon density profile for the ground state of ^{76}Sr.

$$\overline{(**m,**m')^2_\alpha} \equiv \int_{-\infty}^{\infty}\int_{-\infty}^{\infty} dz\, dz' |\chi_m(z)|^2 (z-z')^2 \times e^{-(z-z')^2/s^2} |\chi_{m'}(z')|^2, \tag{A18}$$

$$\overline{(**m)^4_\alpha} \equiv \overline{(**m,**m)^2_\alpha}, \tag{A19}$$

$$(nl*,n'l'*)^2_\alpha \equiv \int\int d^2\rho\, d^2\rho' |\psi_{nl}(\rho,\vartheta)|^2 e^{-(\boldsymbol{\rho}-\boldsymbol{\rho}')^2} | \times \psi_{n'l'}(\rho',\vartheta')|^2, \tag{A20}$$

$$(nl*)^4_\alpha \equiv (nl*,nl*)^2_\alpha, \tag{A21}$$

$$\overline{(nl*,n'l'*)^2_\alpha} \equiv \int\int d^2\rho\, d^2\rho' |\psi_{nl}(\rho,\vartheta)|^2 (\boldsymbol{\rho}-\boldsymbol{\rho}')^2 \times e^{-(\boldsymbol{\rho}-\boldsymbol{\rho}')^2} |\psi_{n'l'}(\rho',\vartheta')|^2, \tag{A22}$$

$$\overline{(nl*)^4_\alpha} \equiv \overline{(nl*,nl*)^2_\alpha}. \tag{A23}$$

The integrals (A16) through (A23) are calculated and tabulated in the same way as the repulsion integrals, only now the integrals are functions of the three parameters: η, ξ, and s. The resultant expressions are rather cumbersome and we do not show them here.

TABLE XVI. Minimization results for ^{72}Kr.

Configuration	B (MeV)	$\hbar\omega_z$ (MeV)	$\hbar\omega_\perp$ (MeV)	β
1	11.58	9.93	11.17	0.14
2	11.49	12.09	10.08	−0.20
3	11.41	10.31	10.94	0.07
4	11.41	10.67	10.69	0.00
5	11.40	11.52	10.24	−0.13

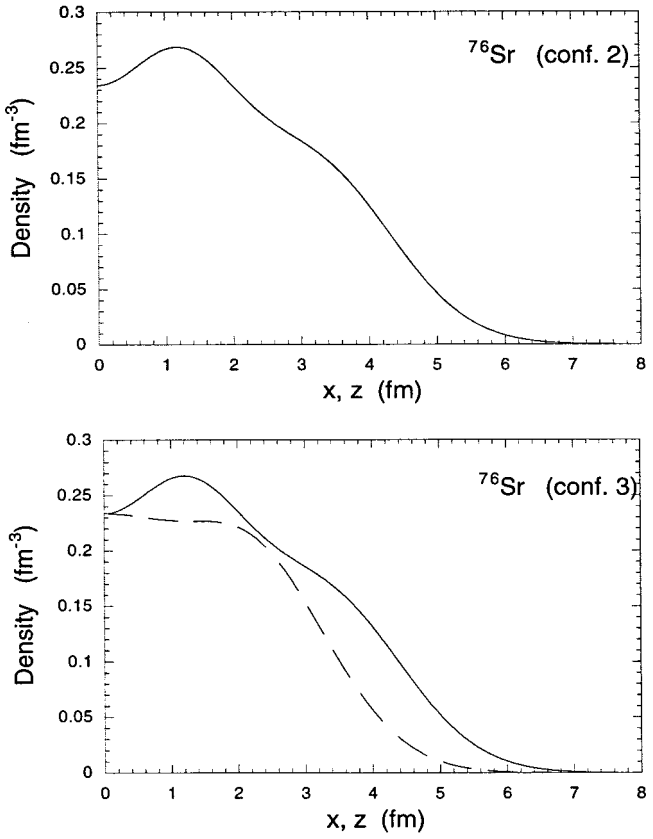

FIG. 50. Nucleon density profile for the first two shape excitations of ^{76}Sr. In the upper picture, the two curves completely overlap.

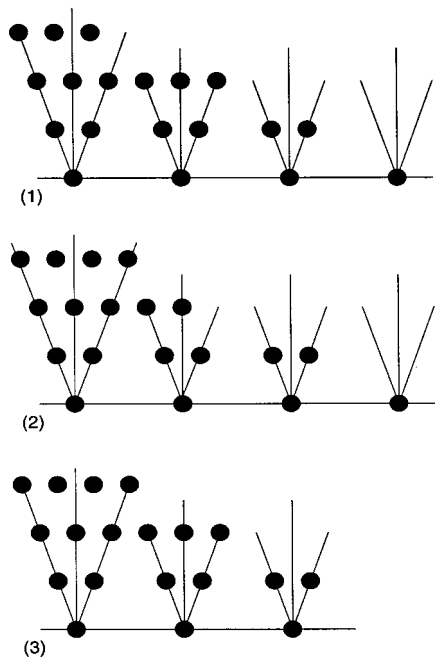

FIG. 51. The first three dot diagrams of ^{76}Sr.

TABLE XVII. Minimization results for ^{76}Sr.

Configuration	B (MeV)	$\hbar\omega_z$ (MeV)	$\hbar\omega_\perp$ (MeV)	β
1	11.87	10.31	10.90	0.06
2	11.83	10.68	10.67	0.00
3	11.83	11.47	10.26	−0.12

The average attractive energy per nucleon can be written now as

$$\langle V_\alpha\rangle = -\frac{1}{A}\alpha C\left[\sum_{m=0}^{M} V_m^{(\mathrm{s.d.})} + \sum_{m'\geqslant m=1}^{M} V_{mm'}^{(\mathrm{d.d.})}\right], \quad \text{(A24)}$$

where in the first term,

$$V_m^{(\mathrm{s.d.})} \equiv 6\sum_{n,l} (nl,m)_\alpha^4, \quad \text{(A25)}$$

the summation is performed over all occupied dots in the mth tree. This term represents the attraction between all pairs of nucleons belonging to the same dot (nl, m). The exact cancelation of the direct and exchange terms reduces the number of terms contributing from one full dot (four nucleons) to $C_2^4=6$. The contribution from pairs where the two nucleons belong to two different dots is given by

$$V_{mm'}^{(\mathrm{d.d.})} \equiv [1-g_s(\langle T\rangle)]\sum_{n,l}\sum_{n',l'} (nlm,n'l'm')_\alpha^2, \quad \text{(A26)}$$

where the summation is extended over all occupied dots in the mth and m'th trees, respectively. It is here that we use the statistical approximation to the exchange energy discussed in Sec. II. Combination of equations (A10) and (A24) gives the entire interaction energy per nucleon for an $N=Z=1/2A$, even-even nucleus.

Let us show how this procedure applies to ^{4}He, the simplest of our nuclei. Its c.m.-corrected average kinetic energy is

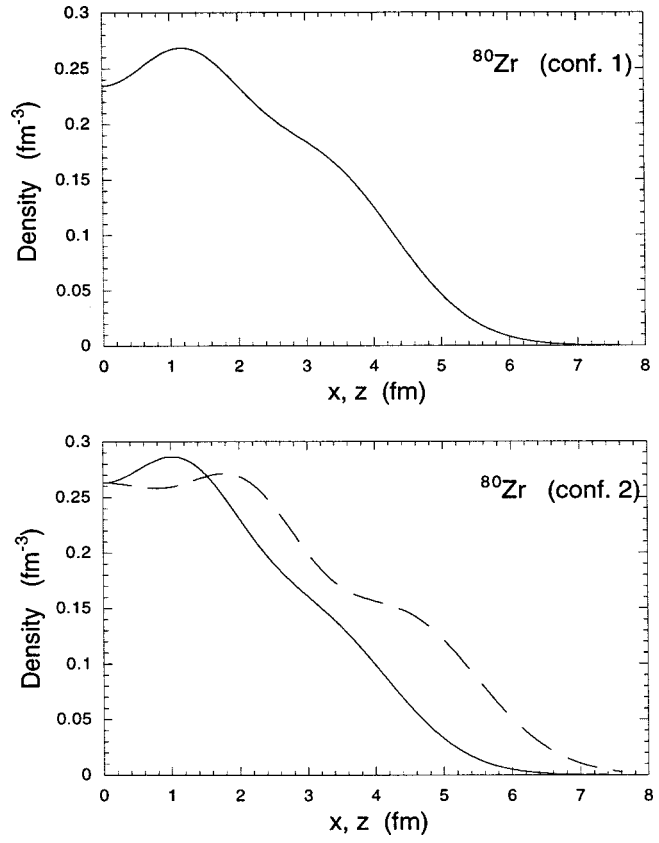

FIG. 52. Nucleon density profile for the ground state and the first shape excitation of ^{80}Zr. In the upper picture, the two curves completely overlap.

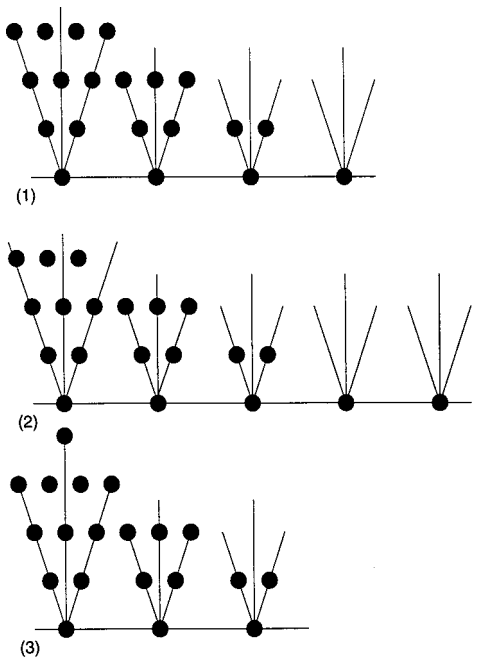

FIG. 53. The first three dot diagrams of ^{80}Zr.

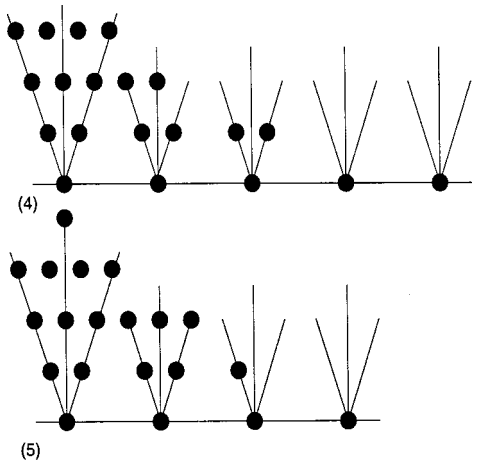

FIG. 54. The next two dot diagrams of ^{80}Zr.

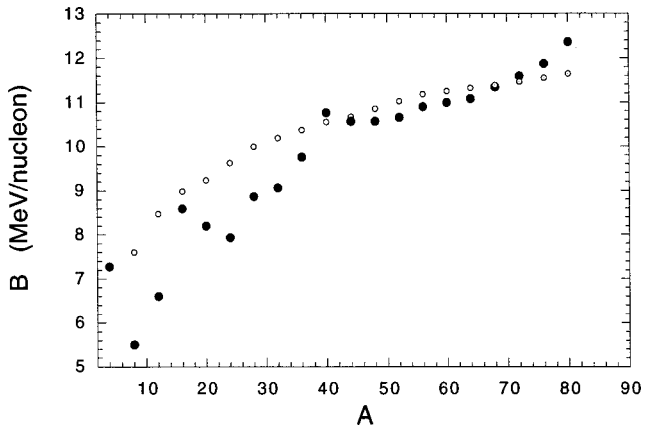

FIG. 55. Calculated ground-state binding energies (full circles) vs the atomic number *A*, compared with corresponding experimental values from Möller *et al.* The last four points of the experimental curve (empty circles with dots) are extrapolated values from the nearest isotope of known mass.

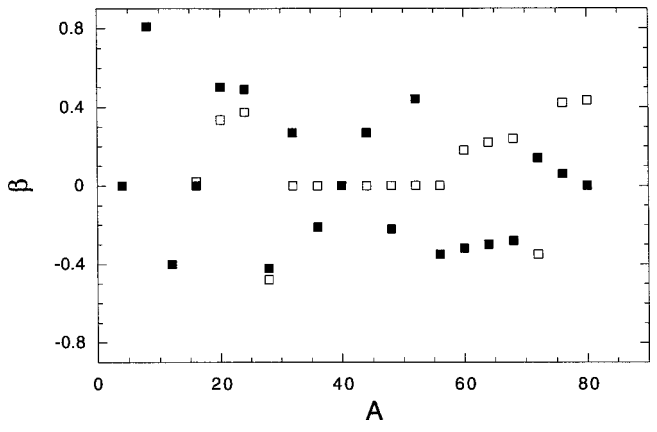

FIG. 56. Calculated ground-state ellipsoidal deformations β (full squares) atomic number *A*. The corresponding calculated values from Möller *et al.* are the empty squares.

TABLE XVIII. Minimization results for ^{80}Zr.

Configuration	B (MeV)	$\hbar\omega_z$ (MeV)	$\hbar\omega_\perp$ (MeV)	β
1	12.36	10.67	10.67	0.00
2	11.85	9.27	11.17	0.22
3	11.75	11.73	9.87	−0.19
4	11.71	9.55	10.96	0.16
5	11.71	11.36	10.05	−0.13

$$\langle T\rangle = \frac{1-\frac{1}{4}}{4}\times 4\times \tfrac{1}{2}(0+\tfrac{3}{2})\hbar\omega = \tfrac{9}{16}\hbar\omega. \qquad \text{(A27)}$$

The average attraction is

$$\langle V_\alpha\rangle = -\tfrac{1}{4}\alpha C V_0^{(\mathrm{s.d.})}, \qquad \text{(A28)}$$

with

$$V_0^{(\mathrm{s.d.})} = 6(00,0)_\alpha^4 = 6[\overline{(00*)_\alpha^4}(**0)_\alpha^4 + (00*)_\alpha^4\overline{(**0)_\alpha^4}]. \qquad \text{(A29)}$$

Let us calculate the integrals:

TABLE XIX. Values of the one-dimensional integrals for the repulsive part of the interaction in the units of $(\eta/2\pi)^{1/2}$.

Orbitals	$(**0)^2$	$(**1)^2$	$(**2)^2$	$(**3)^2$	$(**4)^2$	$(**5)^2$	$(**6)^2$
$(**0)^2$	1	$\frac{1}{2}$	$\frac{3}{8}$	$\frac{5}{16}$	$\frac{35}{128}$	$\frac{63}{256}$	$\frac{231}{1024}$
$(**1)^2$		$\frac{3}{4}$	$\frac{7}{16}$	$\frac{11}{32}$	$\frac{75}{256}$	$\frac{133}{512}$	$\frac{483}{2048}$
$(**2)^2$			$\frac{41}{64}$	$\frac{51}{128}$	$\frac{329}{1024}$	$\frac{569}{2048}$	$\frac{2037}{8192}$
$(**3)^2$				$\frac{147}{256}$	$\frac{759}{2048}$	$\frac{1245}{4096}$	$\frac{4351}{16\,384}$
$(**4)^2$					$\frac{8649}{16\,384}$	$\frac{11\,445}{32\,768}$	$\frac{38\,005}{131\,072}$
$(**5)^2$						$\frac{32\,307}{65\,536}$	$\frac{87\,069}{262\,144}$
$(**6)^2$							$\frac{487\,889}{1\,048\,576}$

TABLE XX. Values of the two-dimensional integrals for the repulsive part of the interaction in the units of $(\xi/2\pi)$.

Orbitals	$(00*)^2$	$(1\pm1*)^2$	$(20*)^2$	$(2\pm2*)^2$	$(3\pm1*)^2$	$(3\pm3*)^2$
$(00*)^2$	1	$\frac{1}{2}$	$\frac{1}{2}$	$\frac{1}{4}$	$\frac{3}{8}$	$\frac{1}{8}$
$(1\pm1*)^2$		$\frac{1}{2}$	$\frac{1}{4}$	$\frac{3}{8}$	$\frac{1}{4}$	$\frac{1}{4}$
$(20*)^2$			$\frac{1}{2}$	$\frac{1}{4}$	$\frac{1}{4}$	$\frac{1}{4}$
$(2\pm2*)^2$				$\frac{3}{8}$	$\frac{3}{16}$	$\frac{5}{16}$
$(3\pm1*)^2$					$\frac{5}{16}$	$\frac{3}{16}$
$(3\pm1*)^2$						$\frac{5}{16}$

Orbitals	$(40*)^2$	$(4\pm2*)^2$	$(4\pm4*)^2$	$(5\pm1*)^2$	$(5\pm3*)^2$	$(5\pm5*)^2$
$(00*)^2$	$\frac{3}{8}$	$\frac{1}{4}$	$\frac{1}{16}$	$\frac{5}{16}$	$\frac{5}{32}$	$\frac{1}{32}$
$(1\pm1*)^2$	$\frac{3}{16}$	$\frac{1}{4}$	$\frac{5}{32}$	$\frac{3}{16}$	$\frac{7}{32}$	$\frac{3}{32}$
$(20*)^2$	$\frac{5}{16}$	$\frac{1}{8}$	$\frac{7}{32}$	$\frac{7}{32}$	$\frac{7}{64}$	$\frac{11}{64}$
$(2\pm2*)^2$	$\frac{5}{32}$	$\frac{3}{16}$	$\frac{15}{64}$	$\frac{9}{64}$	$\frac{25}{128}$	$\frac{21}{128}$
$(3\pm1*)^2$	$\frac{11}{64}$	$\frac{7}{32}$	$\frac{25}{128}$	$\frac{3}{16}$	$\frac{1}{8}$	$\frac{3}{16}$
$(3\pm3*)^2$	$\frac{9}{64}$	$\frac{5}{32}$	$\frac{35}{128}$	$\frac{1}{12}$	$\frac{5}{32}$	$\frac{7}{32}$

Orbitals	$(40*)^2$	$(4\pm2*)^2$	$(4\pm4*)^2$	$(5\pm1*)^2$	$(5\pm3*)^2$	$(5\pm5*)^2$
$(40*)^2$	$\frac{11}{32}$	$\frac{3}{16}$	$\frac{9}{64}$	$\frac{11}{64}$	$\frac{23}{128}$	$\frac{19}{128}$
$(4\pm2*)^2$		$\frac{1}{4}$	$\frac{5}{32}$	$\frac{9}{64}$	$\frac{25}{128}$	$\frac{21}{128}$
$(4\pm4*)^2$			$\frac{35}{128}$	$\frac{15}{128}$	$\frac{35}{256}$	$\frac{63}{256}$
$(5\pm1*)^2$				$\frac{15}{64}$	$\frac{19}{128}$	$\frac{15}{128}$
$(5\pm3*)^2$					$\frac{55}{256}$	$\frac{35}{256}$
$(5\pm5*)^2$						$\frac{63}{256}$

$$(**0)^4_\alpha = \int_{-\infty}^{\infty} dz\, dz' [\chi_0(z)]|^2 |\chi_0(z')|^2 \exp[-(z-z')^2/s^2]$$

$$= \left(\frac{\eta}{\pi}\right) \int_{-\infty}^{\infty} dz\, dz'\, e^{-\eta(z^2+z'^2)} \exp[-(z-z')^2/s^2].$$

With the new variables ζ and Z:

$$z \equiv Z + \tfrac{1}{2}\zeta, \quad z' \equiv Z - \tfrac{1}{2}\zeta, \tag{A31}$$

(A30) Eq. (A30) becomes

$$(**0)_\alpha^4=\left(\frac{\eta}{\pi}\right)\int_{-\infty}^{\infty}d\zeta\,dZ\exp\left[-\eta\left(2Z^2+\frac{1}{2}\zeta^2\right)\right]e^{-\zeta^2/s^2}$$
$$=\left(\frac{\eta}{2}\right)^{1/2}\frac{s}{\sqrt{1+\frac{1}{2}\eta s^2}}. \tag{A32}$$

Similarly,

$$\overline{(**0)_\alpha^4}=\int_{-\infty}^{\infty}dz\,dz'|\chi_0(z)|^2|\chi_0(z')|^2(z-z')^2\epsilon^{-(z-z')^2/s^2}$$
$$=\left(\frac{\eta}{\pi}\right)\int_{-\infty}^{\infty}dz\,dz'\,e^{-\eta(z^2+z'^2)}(z-z')^2e^{-(z-z')^2/s^2}$$
$$=\left(\frac{\eta}{\pi}\right)\int_{-\infty}^{\infty}d\zeta\,dZ\,\zeta^2\exp\left[-\eta\left(2Z^2+\frac{1}{2}\zeta^2\right)\right]e^{-\zeta^2/s^2}$$
$$=\frac{1}{2}\left(\frac{\eta}{2}\right)^{1/2}\frac{s^3}{\left(1+\frac{1}{2}\eta s^2\right)^{3/2}}. \tag{A33}$$

For the two-dimensional integrals, we use the substitution

$$\boldsymbol{\rho}\equiv\mathbf{R}+\tfrac{1}{2}\mathbf{r},\quad \boldsymbol{\rho}'\equiv\mathbf{R}-\tfrac{1}{2}\mathbf{r}. \tag{A34}$$

Then

$$(00*)_\alpha^4=\int d^2\rho\,d^2\rho'|\psi_{00}(\rho,\vartheta)|^2|\psi_{00}(\rho',\vartheta')|^2e^{-(\boldsymbol{\rho}-\boldsymbol{\rho}')^2/s^2}$$
$$=\left(\frac{\xi}{\pi}\right)^2\int d^2\rho\,d^2\rho'\,e^{-\xi(\rho^2+\rho'^2)}e^{-(\boldsymbol{\rho}-\boldsymbol{\rho}')^2/s^2}$$
$$=(2\pi)^2\left(\frac{\xi}{\pi}\right)^2\int_0^{\infty}dr\,r\exp\left[-\left(\frac{1}{2}\xi+\frac{1}{s^2}\right)r^2\right]$$
$$\times\int_0^{\infty}dR\,R\,e^{-2\xi R^2}$$
$$=\left(\frac{\xi}{2}\right)\frac{s^2}{1+\frac{1}{2}\xi s^2}, \tag{A35}$$

and

$$\overline{(00*)_\alpha^4}=\int d^2\rho\,d^2\rho'|\psi_{00}(\rho,\vartheta)|^2|\psi_{00}(\rho',\vartheta')|^2(\boldsymbol{\rho}-\boldsymbol{\rho}')^2$$
$$\times e^{-(\boldsymbol{\rho}-\boldsymbol{\rho}')^2/s^2}$$
$$=\left(\frac{\xi}{\pi}\right)^2\int d^2\rho\,d^2\rho'\,e^{-\xi(\rho^2+\rho'^2)}(\boldsymbol{\rho}-\boldsymbol{\rho}')^2$$
$$\times e^{-(\boldsymbol{\rho}-\boldsymbol{\rho}')^2/s^2}$$
$$=(2\pi)^2\left(\frac{\xi}{\pi}\right)^2\int_0^{\infty}dr\,r^3$$
$$\times\exp\left[-\left(\frac{1}{2}\xi+\frac{1}{s^2}\right)r^2\right]\int_0^{\infty}dR\,R\,e^{-2\xi R^2}$$
$$=\left(\frac{\xi}{2}\right)\frac{s^4}{\left(1+\frac{1}{2}\xi s^2\right)^2}. \tag{A36}$$

Now we have

$$V_0^{(\mathrm{s.d.})}=6s^5\left(\frac{\eta}{2}\right)^{1/2}\left(\frac{\xi}{2}\right)\left[\frac{1}{\left(1+\frac{1}{2}\eta s^2\right)^{1/2}}\,\frac{1}{\left(1+\frac{1}{2}\xi s^2\right)^2}\right.$$
$$\left.+\frac{1}{2}\,\frac{1}{\left(1+\frac{1}{2}\xi s^2\right)}\,\frac{1}{\left(1+\frac{1}{2}\eta s^2\right)^{3/2}}\right]. \tag{A37}$$

For ^{4}He, the two parameters, η and ξ, are equal: $\eta=\xi\equiv\gamma$. Therefore

$$\langle V_\alpha\rangle=-\frac{3}{2}\alpha\left(\frac{\gamma}{2\pi}\right)^{3/2}\frac{1}{\left(1+\frac{1}{2}\gamma s^2\right)^{3/2}}. \tag{A38}$$

(Here, in the limit $s\to 0$, we regain the δ-function result.)

The repulsive energy is

$$\langle V_\beta\rangle=\tfrac{1}{4}\beta\sqrt{\langle T\rangle}\left(\frac{\gamma}{2\pi}\right)^{3/2}\times 6=\frac{9}{8}\beta\left(\frac{\gamma}{2\pi}\right)^{3/2}(\hbar\omega)^{1/2}. \tag{A39}$$

Combining equations (A27), (A38), and (A39), we arrive at the final result, Eq. (29) of Sec. II.

[1] T. H. R. Skyrme, Nucl. Phys. **B9**, 615 (1959).
[2] S. A. Moszkowski, Phys. Rev. C **2**, 402 (1970).
[3] D. Vautherin and D. M. Brink, Phys. Rev. C **5**, 626 (1972).
[4] J. M. G. Gómez, C. Prieto, and J. Navarro, Nucl. Phys. **A549**, 125 (1992).
[5] B. A. Brown, Phys. Rev. C **58**, 220 (1998).
[6] T. Kasahara, Y. Akaishi, and H. Tanaka, Suppl. Prog. Theor. Phys. **56**, 96 (1974).
[7] R. G. Seyler and C. H. Blanchard, Phys. Rev. **124**, 227 (1961); **131**, 355 (1963).
[8] R. V. Reid, Ann. Phys. **50**, 411 (1968).
[9] R. Tamagaki, Prog. Theor. Phys. **39**, 91 (1968).
[10] D. Gogny, P. Pires, and R. De Tourreil, Phys. Lett. **32B**, 591 (1970).
[11] M. Sakai, I. Shimodaya, Y. Akaishi, J. Hiura, and H. Tanaka, Prog. Theor. Phys. **51**, 155 (1974).
[12] B. Friedman and V. R. Pandharipande, Nucl. Phys. **A361**, 502 (1981).
[13] W. D. Myers and W. J. Swiatecki, Nucl. Phys. **A601**, 141 (1996).

[14] H. M. M. Mansour and Kh. A. Ramadan, Phys. Rev. C **57**, 1744 (1998).
[15] J. Meng and P. Ring, Phys. Rev. Lett. **77**, 3963 (1996).
[16] A. W. Pozamantir and A. W. Overhauser, Phys. Rev. C **64**, 014303 (2001), following paper.
[17] A. W. Overhauser (unpublished).
[18] M. Parry and E. Fischbach, J. Math. Phys. **41**, 2417 (2000).
[19] J. P. Blaizot, J. F. Berger, J. Dechargé, and M. Girod, Nucl. Phys. **A591**, 435 (1995).
[20] D. H. Youngblood, H. L. Clark, and Y.-W. Lui, Phys. Rev. Lett. **82**, 691 (1999).
[21] P. Möller, J. R. Nix, W. D. Myers, and W. J. Swiatecki, At. Data Nucl. Data Tables **59**, 185 (1995).
[22] D. Rudolph *et al.*, Phys. Rev. Lett. **82**, 3763 (1999).
[23] T. Tanaka, K. Iwasawa, and F. Sakata, Phys. Rev. C **58**, 2765 (1998).
[24] M. Freer *et al.*, Phys. Rev. Lett. **82**, 1383 (1999).
[25] Frederick Seitz, *Modern Theory of Solids* (McGraw-Hill, New York, 1940), p. 313.
[26] S. M. Fischer, D. P. Balamuth, P. A. Hausladen, C. J. Lister, M. P. Carpenter, D. Seweryniak, and J. Schwartz, Phys. Rev. Lett. **84**, 4064 (2000).
[27] J. L. Wood, K. Heyde, W. Nazarewicz, M. Huyse, and P. van Duppen, Phys. Rep. **215**, 101 (1992).